



Detailed-balance limits for sunlight-to-protonic energy conversion from aqueous photoacids and photobases based on reversible mass-action kinetics

Journal:	<i>Energy & Environmental Science</i>
Manuscript ID	EE-ART-03-2023-000710.R1
Article Type:	Paper
Date Submitted by the Author:	02-Jun-2023
Complete List of Authors:	Phun, Gabriel; University of California, Chemistry Bhide, Rohit; University of California, Chemistry Ardo, Shane; University of California, Chemistry

Detailed-balance limits for sunlight-to-protonic energy conversion from aqueous photoacids and photobases based on reversible mass-action kinetics

Gabriel S. Phun,^{1#} Rohit Bhide,^{1#} and S. Ardo^{1,2,3*}

¹Department of Chemistry, ²Department of Chemical & Biomolecular Engineering, ³Department of Materials Science & Engineering, University of California Irvine, Irvine, CA 92697–2025 USA

these authors contributed equally to this work

* ardo@uci.edu

Broader Context Statement

Absorption of non-equilibrium radiation by photosystems allows them to perform useful work. This is beneficial, because sunlight can be used with, for example, photoelectrochemical devices to drive formation of carbon-neutral/negative fuels. The fundamental physical, chemical, and engineering processes that underlie these light-to-electronic power conversion processes have been studied for over a half-century, and are generally well understood. However, innovative and new photochemical processes, such as those that result in light-to-protonic power conversion, represent emerging concepts that could serve as alternatives to traditional light-to-electronic processes, and with the possibility of economic benefits under certain scenarios. For example, direct sunlight-driven desalination may afford wireless and remote means of clean water generation. Moreover, direct sunlight-driven carbon capture from ocean water could provide an economic pathway to meet the \$100/ton-CO₂ cost target proposed to enable widespread implementation of systems aimed at mitigating the negative effects of global warming. Of primary importance in any new process is the practical efficiency limit. With its knowledge, informed decisions can be made as to scenarios where new energy-conversion processes may provide benefit.

Detailed-balance limits for sunlight-to-protonic energy conversion from aqueous photoacids and photobases based on reversible mass-action kinetics

Gabriel S. Phun,^{1#} Rohit Bhide,^{1#} and S. Ardo^{1,2,3*}

¹Department of Chemistry, ²Department of Chemical & Biomolecular Engineering, ³Department of Materials Science & Engineering, University of California Irvine, Irvine, CA 92697–2025 USA

these authors contributed equally to this work

* ardo@uci.edu

Abstract

Detailed-balance limits to energy conversion critically inform design rules for photochemical power conversion devices. Herein we simulate efficiencies for sunlight-to-protonic power conversion where liquid water serves as the protonic semiconductor and is sensitized to visible-light absorption using reversible photoacids or photobases. Our model includes proton-transfer processes based on the Förster cycle with rate constants that follow the empirical Brønsted relation, where bimolecular reactions are encounter controlled. Based on physically relevant model parameters, simulations of steady-state concentrations of $\text{H}^+(\text{aq})$ and $\text{OH}^-(\text{aq})$ indicate that for defect-free water the maximum possible protonic quasi-chemical potentials result in a photovoltage of ~ 330 mV and a power conversion efficiency of $\sim 10\%$. Conditions of maximum power conversion occur when photoacid (photobase) dyes exhibit acidities (basicities) of $\text{p}K_{\text{a}}$ ($\text{p}K_{\text{b}}$) ≥ 14 and $\text{p}K_{\text{a}}^*$ ($\text{p}K_{\text{b}}^*$) ≤ 0 , an outcome that is nearly independent of equilibrium pH. These conditions are optimal because under standard-state conditions they result in rates for protonation of water to form $\text{H}^+(\text{aq})$ and deprotonation of water to form $\text{OH}^-(\text{aq})$ that are faster than other proton-transfer processes due to their isoergic/exoergic nature. Simulations also indicate that longer excited-state lifetimes result in an increase in the range of $\text{p}K^*$ values that lead to significant protonic quasi-chemical potentials. This occurs because longer excited-state lifetimes up to ~ 1 μs afford more time to perform excited-state proton transfer. Simulation outcomes are affected little by inclusion of empirical nonzero activation free energies for isoergic/exoergic proton-transfer reactions or rate constants for equilibrium radiative generation and recombination of excited-state species under thermal detailed balance. Only when local electric fields are assumed present to

increase rate constants for proton-transfer reactions do protonic quasi-chemical potentials suffer. Simulations also indicate that the total concentration of photoacid/photobase dyes exhibits two competing effects on protonic quasi-chemical potentials. Decreasing dye concentration results in less light absorption and therefore smaller changes in steady-state concentrations of $\text{H}^+(\text{aq})$ and $\text{OH}^-(\text{aq})$, while also increasing the range of $\text{p}K$ values that results in significant changes in quasi-chemical potentials. Overall, these results define parameters for effective sunlight-to-protonic power conversion and will help guide researchers in the design and development of photoacid/photobase dyes for light-driven proton pumps.

Introduction

Electrons and protons are both charged elementary particles with interactions in phases that are dominated by the electromagnetic force. Therefore, theories used to calculate potential energy surfaces, rates of charge-transfer reactions, and flux of electrostatically-driven transport (drift/migration) are the same for both electrons and protons. This suggests that models for solar energy conversion based on *electronic processes* in photovoltaics and solar fuels constructs are also applicable to *protonic processes* in sunlight-driven proton pumps. While most reports of proton pumps driven by visible light are modeled after biological systems whose mechanisms differ significantly from their electronic counterparts, recent efforts from our group¹⁻⁶ have taken the new approach of designing and analyzing visible-light-driven proton pumps based on knowledge gained from the solid-state-physics electronic semiconductor and photovoltaic communities since their pioneering efforts in the 1940s – 1950s.⁷⁻¹⁰ This approach supports the need to quantify the detailed-balance limit for conversion of sunlight into protonic, or more generally ionic, power.

Theoretical photoinduced power conversion efficiency limits for electronic solar photovoltaic devices performing electric work across a hypothetical resistive load were first reported by Shockley and Queisser in 1961.¹¹ Their theory assumed voltage and current generation from sunlight absorption by ideal electronic semiconductor diodes with a defined onset wavelength/energy for photon absorption, i.e. the electronic bandgap, that resulted in complete absorption of photons with energy greater than this value and lossless charge separation and collection. Moreover, they approximated thermally equilibrated Fermi–Dirac and Bose–Einstein–Planck distributions as Maxwell–Boltzmann distributions, due to the assumption of low-intensity solar insolation and nondegenerate doping of the semiconductor. This thermal detailed-balance limit was derived for any general photochemical process by Ross and Hsiao in 1977,¹² using the thermodynamically rigorous physical parameter of chemical potential. While not explicitly invoking the presence of an ideal semiconductor diode, the same outcomes resulted, because of their analogous assumptions that no chemical potential was lost as heat in the process of driving hypothetical processes with an optimal free energy load, such as (electro)chemical reactions or electric current. To determine the maximum change in chemical potential of the population of excited-state species that was available to perform useful work, like the photovoltaic models, Ross and Hsiao assumed that their two-electronic-state system was initially in thermal equilibrium with the surroundings, i.e. in the dark. The condition of thermal equilibrium requires equal rates of generation and recombination of excited-state species via absorption and emission, respectively, of ambient blackbody photons with energy greater than, or equal to, a predefined onset for photon absorption, i.e. the electronic gap between the highest occupied and lowest unoccupied molecular orbitals. For this photochemical model to be applicable to an ensemble of individual reaction centers, such as a collection of molecular dyes, the species populations in the ground state and the

species populations in the excited state were each assumed to rapidly reach thermal and quasi-chemical equilibrium¹³ based on statistical mechanics in the long-time-averaged ergodic limit. Calculated photoinduced changes in chemical potential were identical to their electric work counterparts resulting from the photovoltaic model, thus providing a theoretical bridge between concepts in solid-state-physics electronic photovoltaics and molecular photochemistry.¹⁴ This general photochemical model was expanded by Bolton, et al.^{15,16} to include non-zero hypothetical electrochemical losses. These losses were in the form of realistic overpotentials for the redox reactions, for example, the two half-reactions that constitute water splitting, such that some of the photogenerated chemical potential was lost as heat in order to drive the redox reactions at a sufficient rate. A variety of chemical load curves can be evaluated using this modeling framework to capture other processes such as generation of ionic power through photo-ionization processes or photochemical reactions initiated by proton-transfer processes. However, none of these thermal detailed-balance models incorporated fundamental chemical kinetics based on microscopically reversible mass action. By omitting such rigorous chemical detailed-balance conditions, these models decoupled the concentration of photogenerated species from their chemical reactivity, which is inaccurate.

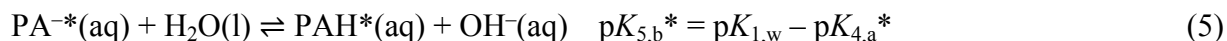
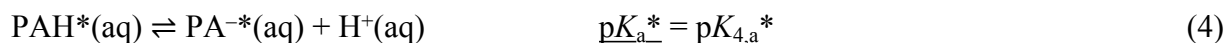
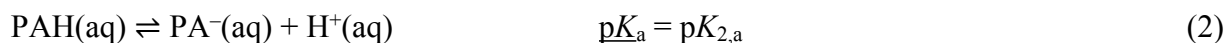
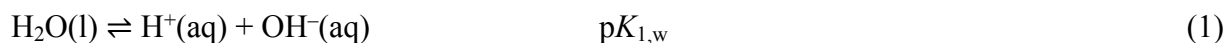
Herein we report results from a photochemical detailed-balance analysis to determine maximum theoretical sunlight-to-protonic power conversion from a collection of reversible photoacid/photobase dyes that undergo well-known excited-state proton-transfer (ESPT) reactions, based on their thermodynamic driving forces, concentrations, and excited-state lifetimes. However, unlike prior works, we do not vary the hypothetical onset for photon absorption by such molecular dyes and instead we assume that dyes are near-optimal based on their purpose of sensitizing proton-transfer reactions with water species (i.e. $\text{H}_2\text{O}(\text{l})$, $\text{H}^+(\text{aq})$, and

OH⁻(aq)) to visible light. We do, however, vary the thermodynamics of these reactions, and therefore also their rate constants, to understand the influence that fundamental ESPT *reactivity*, not *absorbance*, has on sunlight-to-protonic power conversion. Our model includes validated rate constants for thermodynamically favorable bimolecular proton-transfer reactions,¹⁷ which are assumed to either be encounter controlled¹⁸ or exhibit a relationship that follows Marcus theory.^{19–}
²¹ Rate constants for opposing reactions, which include unimolecular reactions or thermodynamically unfavorable bimolecular reactions, are determined in accordance with the equilibrium constant (K) being equal to the ratio of the forward and backward rate constants, k_f and k_b , respectively. Unlike prior thermal detailed-balance models, equations used in our model cannot be solved analytically because of bimolecular reactions between molecular dyes and H⁺(aq) or OH⁻(aq), which therefore required us to use continuum-level simulations to evaluate the different model conditions.

Experimental

The modeling framework is based on spatially-invariant reactions that follow the law of mass action. Processes for species-selective charge separation and collection are not included in the model, because they represent well-understood additional losses on top of limits obtained from detailed-balance analyses and strategies for their effective design and implementation are known, which is explained in greater detail in the Supplementary Information. Notwithstanding, our parameter choices are consistent with conditions that afford effective separation and collection of mobile protonic charged species. We define the activity of each species in the model to be equal to its respective concentration, and the activity of water to be unity and therefore with a chemical potential $\mu_{\text{H}_2\text{O}} = \mu^{\circ}_{\text{H}_2\text{O}}$, which we define to be equal to zero. By analogy to the reversible hydrogen

electrode in electrochemistry, at thermal and chemical equilibrium we define a pH-independent $\mu_{\text{H}^+} = 0$, which by the definition for autoprotolysis equilibrium ($\mu_{\text{H}_2\text{O}} = \mu_{\text{H}^+} + \mu_{\text{OH}^-}$) means that $\mu_{\text{OH}^-} = 0$. This convention was chosen so that changes in chemical potential for protonic water species, i.e. $\text{H}^+(\text{aq})$, $\text{OH}^-(\text{aq})$, and $\text{H}_2\text{O}(\text{l})$, could be simplified to $\Delta\mu_{\text{H}^+} = \mu_{\text{H}^+}$, $\Delta\mu_{\text{OH}^-} = \mu_{\text{OH}^-}$, and $\Delta\mu_{\text{H}_2\text{O}} = 0$, respectively, and that analogous to electronic semiconductors, the total change in chemical potential for protonic water species as $\mu_{\text{H}^+} + \mu_{\text{OH}^-}$ represents the maximum amount of useful work that can be performed. All possible proton-transfer reactions between ground-state photoacids/photobases (PAH/PA^-), thermally equilibrated electronic excited state photoacids/photobases ($\text{PAH}^*/\text{PA}^{-*}$), and protonic water species are considered,²² and with the indicated equilibrium constants, K , as follows,



where $\text{p}X$ equals $-\log(X)$, and $K_{1,\text{w}}$ is the autoprotolysis equilibrium constant of water and is set equal to the value at 25 °C of 10^{-14} , $K_{i,\text{a}}$ is the Brønsted–Lowry acid dissociation equilibrium constant of reaction i , and $K_{i,\text{b}}$ ($= K_{1,\text{w}}/K_{i,\text{a}}$) is the Brønsted–Lowry base dissociation equilibrium constant of reaction i . As indicated above via underlined text, to simplify discussion of these relations, below we exclusively indicate the thermodynamic properties of **Reactions 2 and 3** using $\text{p}K_{\text{a}}$, **Reactions 4 and 5** using $\text{p}K_{\text{a}}^*$, and **Reaction 6** using $\Delta\text{p}K = \text{p}K_{\text{a}}^* - \text{p}K_{\text{a}}$.

For the base-case model, bimolecular proton-transfer reactions involving $\text{H}^+(\text{aq})$, $\text{OH}^-(\text{aq})$, photoacid species, and/or photobase species, but not $\text{H}_2\text{O}(\text{l})$, are reasonably assumed to occur at encounter-controlled rates with diffusion-limited rate constants, $k_{i,\text{dl}}$ (**Table 1**). This implies that isoergic reactions, whose standard Gibbs free energy difference, ΔG° , equals zero, have little-to-no standard Gibbs free energy of activation, ΔG^\ddagger .¹⁸ This assumption is equivalent to having a Brønsted slope equal to zero for these bimolecular reactions (backward direction of **Reactions 1** **Table 1. Second-order diffusion-limited rate constants, $k_{i,\text{dl}}$, used in the base-case model.**

Reaction Number(s) and Direction(s) (f)orward, (b)ackward	Reactants	$k_{i,\text{dl}}$
1b	$\text{H}^+(\text{aq}) + \text{OH}^-(\text{aq})$	$1.1 \times 10^{11} \text{ M}^{-1} \text{ s}^{-1}$
2b, 4b	$\text{PA}^-/\text{PA}^{*}(\text{aq}) + \text{H}^+(\text{aq})$	$3 \times 10^{10} \text{ M}^{-1} \text{ s}^{-1}$
3b, 5b	$\text{PAH}/\text{PAH}^*(\text{aq}) + \text{OH}^-(\text{aq})$	$1.8 \times 10^{10} \text{ M}^{-1} \text{ s}^{-1}$
6f or 6b	$\text{PAH}/\text{PAH}^*(\text{aq}) + \text{PA}^-/\text{PA}^-(\text{aq})$	$3 \times 10^9 \text{ M}^{-1} \text{ s}^{-1}$

– **5**) and a Brønsted slope equal to one for the opposite reactions (forward direction of **Reactions 1 – 5**).¹⁸ Second-order encounter-controlled diffusion-limited rate constants used in the model are those reported previously for the backward direction of **Reaction 1**,^{18,23} while for the backward direction of **Reactions 2 – 5**, and the thermodynamically favorable direction for **Reaction 6**, values are approximated by scaling the average experimentally determined rate constant for the reverse of ESPT from a series of photoacids (backward direction of **Reaction 4**) of $k_{4,\text{dl}} \approx 3 \times 10^{10} \text{ M}^{-1} \text{ s}^{-1}$,¹⁷ using $k_{i,\text{dl}} = k_{4,\text{dl}} \left(\frac{D_{i,\text{A}} + D_{i,\text{B}}}{D_{\text{H}^+} + D_{\text{PAH}/\text{PA}^-}} \right)$, where $D_{i,\text{A}}$ and $D_{i,\text{B}}$ stand for diffusion coefficients for the two species, A and B, involved in the bimolecular reaction, i ($D_{\text{H}^+(\text{aq})} = 9.31 \times 10^{-5} \text{ cm}^2/\text{s}$,²⁴ $D_{\text{OH}^-(\text{aq})} = 5.27 \times 10^{-5} \text{ cm}^2/\text{s}$,²⁴ and $D_{\text{PAH}(\text{aq})} = D_{\text{PA}^-(\text{aq})} = 5 \times 10^{-6} \text{ cm}^2/\text{s}$ ^{25–27}). Using these values of $k_{i,\text{dl}}$ and the equilibrium constant for each reaction, $K_i = 10^{-\text{p}K_i}$, the unknown rate constant for the reaction in the other direction is computed, $k_{i,\text{nondl}} = K_i \times k_{i,\text{dl}}$. Alternative assumptions that more accurately replicate empirical observations are implemented and discussed in the Results and Discussion Section and Supplementary Information. These include use of driving-force-dependent rate constants for bimolecular reactions that are consistent with Marcus bond-energy–bond-order

(BEBO) theory,^{28,29} and use of electric-field-enhanced rate constants for thermodynamically unfavorable charge-forming reactions that are consistent with the second Wien effect.^{30–32}

Processes that involve absorption or emission of light are considered, and with the indicated excited-state lifetimes, τ_i , as follows,



where ** stands for a doubly electronic excited state that were only introduced for mass balance of **Reactions 9 and 10**, and are species that are not actually included in the model because their excited-state lifetimes are assumed to be zero. The total rate of photon absorption by all photoacid or photobase species is calculated by assuming 90% absorption of air mass 1.5G solar photons at 1 Sun irradiance (100 mW cm^{-2})³³ with energy greater than, or equal to, that of the protonic gap of water, previously described as being $\sim 1.035 \text{ eV}$ ($\sim 1200 \text{ nm}$).² This leads to an absorbed photon fluence rate, $I_{\text{solar}_{\text{abs}}} = 480 \text{ nmol photon cm}^{-2} \text{ s}^{-1}$, which in charge flux units is equal to 46.4 mA cm^{-2} . The protonic gap of water, which equals $E_{00,7}$ for photoacids and $E_{00,8}$ for photobases, was approximated using the standard solid-state-physics equation for the bandgap energy, E_g , of an electronic semiconductor,³⁴

$$E_g = -k_B T \ln (n_i^2 / (N_c N_v)) \approx -k_B T \ln (K_{1,w} / [\text{H}_2\text{O}]^2) \quad (11)$$

where k_B is the Boltzmann constant ($1.381 \times 10^{-23} \text{ J K}^{-1}$), T is the temperature and is assumed to be equal to 298.15 K , n_i is the intrinsic carrier density, N_c is the effective density of states in the conduction band, N_v is the effective density of states in the valence band, $[\text{H}_2\text{O}]$ is the concentration

of water (55.5 M), and dimensions for the values in the logarithm are chosen so that the expression in the logarithm is dimensionless. Even though the model is spatially zero-dimensional, an optical pathlength over which light is absorbed, $\ell = 10$ nm, is assumed so that areal rates of photon absorption can be converted into average volumetric reaction rates, via division by ℓ . This value for ℓ is the approximate thickness of space-charge regions in state-of-the-art bipolar ion-exchange membranes^{6,32,35} that are responsible for charge separation in our previously reported visible-light-driven proton pumps.^{2,4,6} Moreover, the model assumes spatially invariant rates of photon absorption and subsequent reactions. For the base-case model we assume excited-state lifetimes, $\tau_{7,\text{PAH}^*} = \tau_{8,\text{PA}^{-*}} = 5$ ns, for all singly-excited photoacid and photobase species, because this is the approximate excited-state lifetime of several well-known visible-light-absorbing organic photoacid and photobase dyes (**Table S1**).^{36–38} The similarity between these excited-state lifetimes and the average time it takes for a proton to diffuse over ℓ ($t_{\text{diff}} = \ell^2/D = (10^{-6} \text{ cm})^2 / (9.31 \times 10^{-5} \text{ cm}^2 \text{ s}^{-1}) = 10$ ns) means that excited-state chemical potentials will be approximately spatially homogeneous, and therefore that spatial homogenization of photoexcitation events is a reasonable approximation. This assumption is further bolstered by the fact that large electric fields are likely to be present, which will drive charge separation more quickly and over larger distances during this time, and that photogenerated protons and hydroxides recombine on much larger timescales than the excited-state lifetime of photoacids.⁵

For the base-case model, we also assume a reasonable, but large, total dye concentration, $c_{\text{total}} = 1 \text{ M} = [\text{PAH}] + [\text{PA}^-] + [\text{PAH}^*] + [\text{PA}^{-*}]$, which herein is only ever decreased in value for parametric analyses. This concentration is a reasonable upper limit, because it is equivalent to 1 molecule every 1.66 nm^3 , and that is the approximate size of a photoacid or photobase molecule. Assuming a cube-shaped volume, this results in ~ 8 molecules over our chosen optical pathlength

of 10 nm. While such a small number may warrant the use of simulations based on stochastic kinetic Monte Carlo analyses, outcomes are likely to be the same as those obtained using continuum-level models like that used herein.^{13,39} We also assume for the base-case model a wavelength-independent and species-independent molar decadic absorption coefficient. We also assume for the base-case model a wavelength-independent and species-independent molar decadic absorption coefficient, $\varepsilon = 10^6 \text{ M}^{-1} \text{ cm}^{-1}$, for photons with energy greater than, or equal to, that of the protonic gap of water, and zero elsewhere. This results in a wavelength-independent absorbance from all dye species, $\text{Abs}_{\text{total}} = (\varepsilon c_{\text{total}} \ell) = 1$ or 0 , respectively, that then satisfies our assumption that 90% of incident sunlight with energy greater than, or equal to, that of the protonic gap of water is absorbed. This value for ε is a reasonable upper limit assuming strongly absorbing photoacids/photobases based on molecules like porphyrins or nanomaterials like quantum dots,^{40–42} and the assumption of a wavelength-independent value for ε is a common simplification made in models used to calculate detailed-balance power conversion efficiency limits.^{11,12,15,16} We also assume that no incident light is reflected, because antireflective coatings are well-understood and effective, multiple reflections are challenging to simulate, and reflection losses are presumed small. By choosing ε to be independent of photoacid or photobase species, the model captures approximate effects due to competitive light absorption by excited-state species, which are not modeled to undergo any photochemical processes (**Reactions 9 and 10**), e.g. due to very rapid nonradiative generation and recombination of doubly electronic excited-state photoacid and photobase species, but are still parasitic to sunlight-to-protonic power conversion by decreasing the amount of light absorbed by ground-state photoacid and photobase species.⁴³ Moreover, under no simulation conditions were species initially in their ground state depleted by >10%, ensuring that the impractical condition of population inversion was not approached, or else stimulated

emission must be included in the model, and it was not. This upper limit to the percentage of dyes in their excited state also limits the extent of competitive light absorption by excited-state species to this same small amount.

Rates of absorption of solar photons by PAH via **Reaction 7** and by PA⁻ via **Reaction 8** are based on [PAH] and [PA⁻], respectively, and are determined as follows, with a detailed derivation in the Supplementary Information,

$$\text{Rate}_{if} = \frac{I_{\text{solar}_0}}{\ell} \left(\frac{[Y]}{c_{\text{total}}} \right) \left(1 - 10^{-\left(\epsilon c_{\text{total,effective}} \ell \right)} \right) \quad (12)$$

where I_{solar_0} is the incident photon fluence rate (mol photon cm⁻² s⁻¹), Y = PAH or PA⁻, and $c_{\text{total,effective}} = c_{\text{total}}$, except in the case where effects due to c_{total} and $\text{Abs}_{\text{total}}$ are decoupled and in which case $c_{\text{total,effective}} = 1$ M. By not explicitly defining in the model additional reactions for nonradiative generation and recombination of excited-state photoacid and photobase species, the photoluminescence quantum yield is assumed to be unity, which is not the case observed experimentally.¹ However, these details do not influence simulation results, because inner filter effects⁴⁴ due to inter-dye photon recycling and energy transfer are also not included in the base-case model, and generation and recombination of H⁺(aq) and OH⁻(aq) via **Reaction 1** are assumed to be nonradiative, which is a reasonable assumption because $k_{1,\text{nondl}}$ (= 1.1 × 10⁻³ M/s, which over 10 nm equals ~10⁻¹² mol cm⁻² s⁻¹ = 10⁻⁷ A cm⁻²) is >8 orders-of-magnitude larger than a realistic rate of equilibrium radiative generation and recombination at ambient temperature.¹¹

Generation and recombination of excited-state photoacid and photobase species by equilibrium thermal processes, including radiative and nuclear (nonradiative) heat transfer, are not included in the base-case model, because in practice generation of excited-state photoacid and photobase species require substantially more energy than predicted by ΔpK_a . Typical values of the

standard Gibbs free energy difference to the excited state for photoacids, $\Delta G^{\circ}_7 (\approx E_{00,7})$, and photobases, $\Delta G^{\circ}_8 (\approx E_{00,8})$, are ≥ 2.5 eV, meaning that when 1 M ground-state species are present, $<10^{-42}$ M excited-state species (or $\ll 1$ excited-state species per km^3) are present at thermal equilibrium. Even assuming the protonic gap of water of ~ 1.035 eV, $<2,000$ excited-state species per mL would be present at thermal equilibrium, which are excited-state concentrations that are too small to influence simulation results. Rigorous thermal detailed-balance conditions, which include generation and recombination of excited-state photoacid and photobase species by thermal processes, are implemented and discussed in the Results and Discussion Section and Supplementary Information. Moreover, in the base-case model, we only consider $\text{H}^+(\text{aq})$ and $\text{OH}^-(\text{aq})$ to be mobile charge carriers that can perform useful work, implying that quantification of photoinduced changes in chemical potential of photoacid and photobase species is not necessary in order to accurately quantify the amount of useful work that can be performed.

The modeling framework was implemented in COMSOL Multiphysics 5.3 using the Chemical Reaction Engineering Module to perform finite-element simulations. The temperature is held constant at 298.15 K and initial concentrations for protons and hydroxides are set equal to $10^{-\text{pH}}$ M and $10^{-\text{pOH}}$ M, respectively. For the base-case model that did not satisfy thermal detailed balance, initial concentrations of excited-state photoacid and photobase species are set equal to zero and therefore initial concentrations of ground-state photoacid and photobase species at chemical equilibrium are accurately determined using the Henderson–Hasselbalch equation and c_{total} , as follows,

$$[\text{PAH}] = c_{\text{total}} - [\text{PA}^-] = \frac{c_{\text{total}}}{1 + 10^{(\text{pH} - \text{p}K_{\text{a}})}} \quad (13)$$

No counterions are included in the model, which is inconsequential to simulation results because activity coefficients are assumed to be unity and the spatially zero-dimensional model does not account for electric-field-driven transport via migration/drift. For the base-case model we assume that $\tau_{7,\text{PAH}^*} = \tau_{8,\text{PA}^*} = 5$ ns and $c_{\text{total}} = 1$ M, yet each of these variables was also systematically parametrized in order to determine its influence on the amount of useful work that can be performed due to H^+ and/or OH^- . A time-dependent solar-simulated light pulse was implemented using COMSOL's rectangle function with a lower limit of 1 s, upper limit of 2 s, transition zone of 0.001 s, and 2 continuous derivatives. COMSOL's parametric sweep function was used to parametrize variables and each condition was analyzed using a time-dependent study with a relative tolerance of 10^{-10} , physics control of the initial values of all dependent variables, a time step of 0.001 s, and termination 1 s after initiating the illumination event. The time-dependent solver was MUMPS with automatic row reordering, and use of row equilibration and the automatic setting for matrix symmetry, matrix format, and null space function. The automatic Newton nonlinear method was used with an initial damping factor of 1, minimum damping factor of 10^{-4} , restriction size for update of 10, and automatic use of recovery damping factor of 0.75. Tolerance was used as the criterion for termination with a tolerance factor of 10^{-5} . Herein, sums of the steady-state chemical potentials for $\text{H}^+(\text{aq})$ and $\text{OH}^-(\text{aq})$ are termed total protonic quasi-chemical potentials and are reported as mean values, with negligible standard deviations for the base-case models (**Figure S1a,b,c**). These mean and standard deviation values were determined using propagation of uncertainty based on values for the mean and standard deviation of the steady-state concentrations of H^+ and OH^- obtained at 0.3, 0.4, 0.5, 0.6, and 0.7 s after initiation of light excitation.

Results and Discussion

Photochemical energy conversion relies on several elementary reaction steps that each occur simultaneously, and reversibly, during illumination of an ensemble of dyes by an external light source. When this illumination is constant, a steady-state condition results and the system is said to be at detailed balance, where rates of photon absorption, and thus excited-state generation, and the combined rates of excited-state recombination and energy conversion are equal. Under this condition, concentrations, and thus activities and chemical potentials, of some species are necessarily perturbed from values present in the initial state of the system, forming a state that is not at chemical equilibrium and can perform useful work. Our system starts at equilibrium, and absorption of simulated sunlight changes the concentration of each of the four photoacid or photobase species, as well as the concentration of H^+ and OH^- , by what is termed the Förster cycle (**Figure 1a**). Because H^+ and OH^- are highly mobile charged species in many phases, in practice they can most easily be collected at selective contacts to perform useful work, such as when they are incorporated into an ionic diode that possesses a built-in space-charge region^{2,4-6} or a depletion region that transiently forms due to species transport.^{3,45,46} Useful work due to H^+ and/or OH^- includes processes, such as, directly altering the concentration of reactants and/or products of a reversible chemical reaction involving H^+ and/or OH^- (e.g. H_2 evolution, O_2 evolution, CO_2 reduction, N_2 reduction, $\text{HCO}_3^-/\text{H}_2\text{CO}_3$ dehydroxylation/dehydration), modifying equilibrium electric potential differences to affect transport of all mobile charged species and separate them based on their charge (e.g. electrodialysis, ion separations), altering the chemical potential of water thereby affecting colligative processes (e.g. forward osmosis, condensation, melting). Agnostic to the ultimate use of non-equilibrium steady-state chemical potentials for H^+ and/or OH^- , knowledge of their changes under solar irradiation allows for prediction of maximum possible photoinduced

power conversion efficiencies. Therefore, herein we primarily report on how thermodynamic and kinetic parameters of the system influence steady-state chemical potentials for $\text{H}^+(\text{aq})$ and $\text{OH}^-(\text{aq})$ when simulated to be illuminated by sunlight.

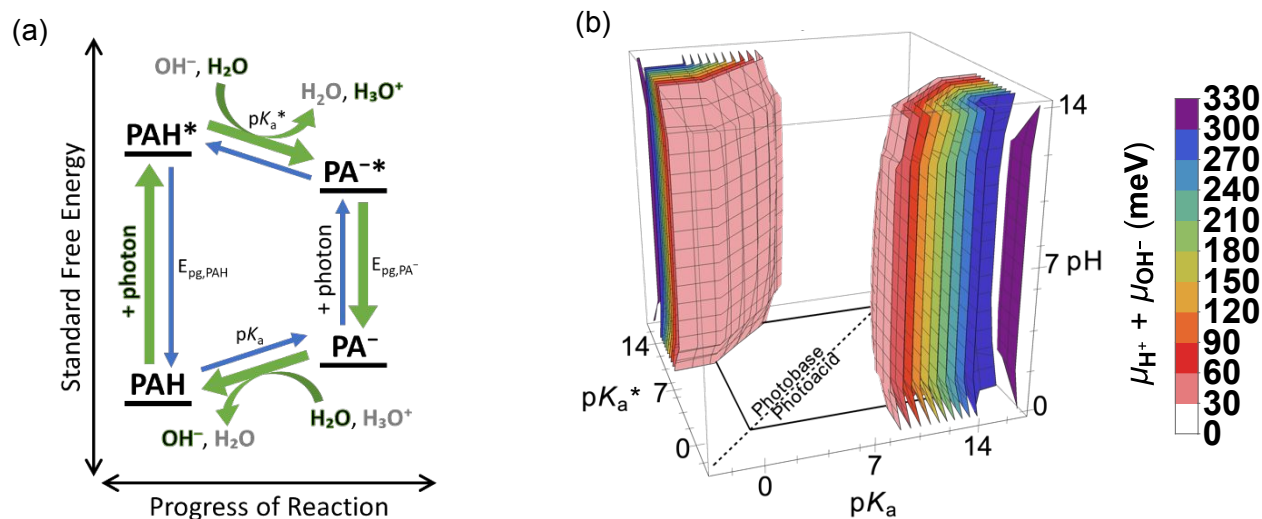


Figure 1. (a) Standard free energy diagram showing the reversible steps in the Förster cycle for sunlight-to-protonic power conversion, assuming standard-state concentrations of $[\text{H}^+]_o = [\text{OH}^-]_o = \sqrt{K_w} = 10^{-7} \text{ M}$. An optimized photoacid dye (with $\text{p}K_a > \sim 14$ and $\text{p}K_a^* < \sim 0$) will photogenerate both $\text{H}^+(\text{aq})$ and $\text{OH}^-(\text{aq})$ from water (bold text with green outline), resulting in net heterolytic water dissociation. (b) Three-parameter contour plot of the sum of the steady-state quasi-chemical potentials for protons and hydroxides ($\mu_{\text{H}^+} + \mu_{\text{OH}^-} - \mu_{\text{H}_2\text{O}}$, with $\mu_{\text{H}_2\text{O}} = 0$) as a function of $\text{p}K_a$, $\text{p}K_a^*$, and equilibrium pH.

Effects of thermodynamic parameters on sunlight-to-protonic photochemical energy conversion

In order to most clearly illustrate results from this multidimensional model, initial parametric analyses were conducted by holding constant parameters related to total concentration/mass of photoacid and photobase species (i.e. total dye concentration, $c_{\text{total}} = 1 \text{ M}$, with initial speciation of protonated and deprotonated ground-state species via chemical equilibration based on pH) and sunlight-driven generation rate and recombination rate of excited-state photoacid and photobase species (total absorbance = 90% ($\text{Abs}_{\text{total}} = 1$) with absorption shared among all four protonated and deprotonated ground-state and excited-state species, each assumed to have the same wavelength-independent absorption coefficient, and excited-state lifetimes for each of the

protonated and deprotonated excited-state species, $\tau_{7,PAH^*} = \tau_{8,PA^{*-}} = 5$ ns). Parameters that were altered were those related to system thermodynamics, which influence many of the photoacid and photobase kinetic parameters, each over up to 20 orders-of-magnitude (i.e. equilibrium pH = [0, 14], $pK_a = [-3, 17]$, $pK_a^* = [-3, 17]$, each by steps of one) (**Figure 1b**). Notably, microenvironments influence thermodynamic parameters, such as species standard chemical potential and spatial electric potential, resulting in nonunity partition coefficients between adjacent microenvironments. For the case of photoacids and photobases, this alters pK_a values,³ which are captured in our results by considering that simulated pK_a values represent those measured *in situ*. Moreover, in subsequent parametric analyses, mass and kinetic variables for photoacid and photobase species were parametrized while holding constant optimal or representative thermodynamic values.

In order to more clearly interpret the three-parameter contour plot shown in **Figure 1b**, representative results are shown as two-parameter contour plots in **Figure 2a,b,c** for the cases of equilibrium pH = 0, pH = 7, and pH = 14. It is clear from these results that photoacidic behavior ($pK_a > pK_a^*$) and photobasic behavior ($pK_a < pK_a^*$) as a function of pK_a and pK_a^* are very similar about the condition of $pK_a = pK_a^*$, which is unsurprising based on the use of analogous kinetic equations, and parameters that are approximately the same, for photoacids and photobases. Slight asymmetries do exist in the data due to differences in D_{H^+} and D_{OH^-} , which affect the second-order diffusion-limited rate constants (**Table 1**). These similarities also result in nearly identical observations when equilibrium pH = 0 or pH = 14 and collectively indicate that photoacids are most effective at performing useful work when $pK_a \geq 14$ and $pK_a^* \leq 0$, while photobases are most effective at performing useful work when their protonated conjugate acids exhibit $pK_a \leq 0$ and $pK_a^* \geq 14$. When cast in terms of general pK , representing pK_a for photoacids and pK_b for

photobases ($pK_b = pK_{\text{Lw}} - pK_a$, with $pK_{\text{Lw}} = 14$), each of these conditions can be succinctly written as $pK \geq 14$ and $pK^* \leq 0$, meaning $\Delta pK (= pK^* - pK) \leq -14$.

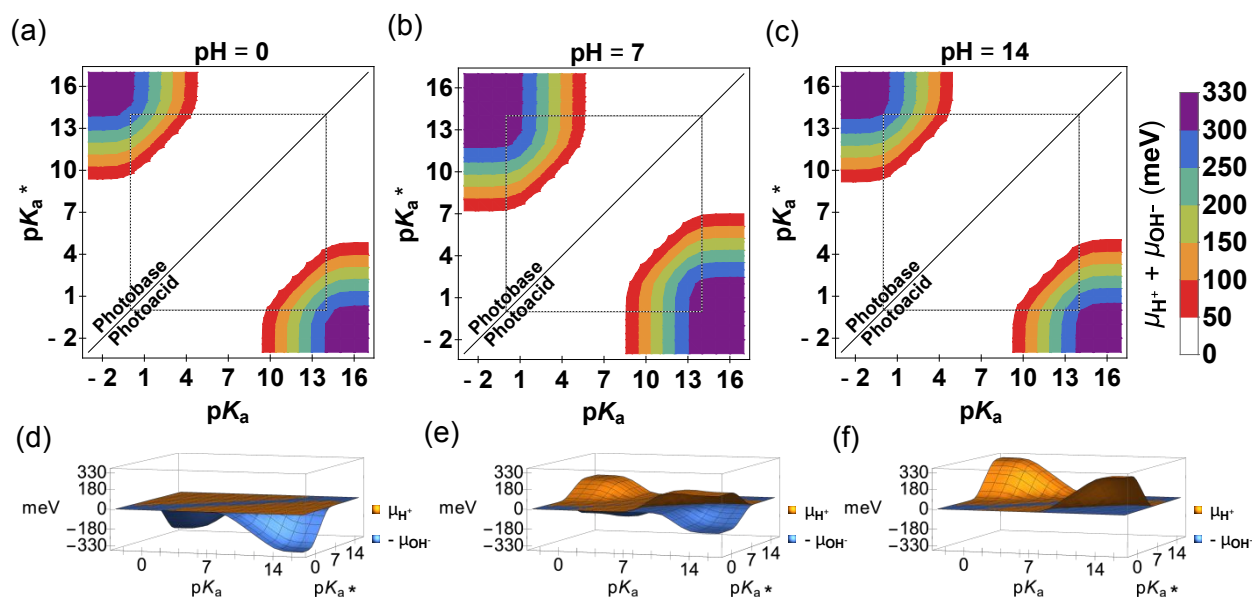


Figure 2. Top Row: Contour plots of the sum of the steady-state quasi-chemical potentials for protons and hydroxides ($\mu_{\text{H}^+} + \mu_{\text{OH}^-} - \mu_{\text{H}_2\text{O}}$, with $\mu_{\text{H}_2\text{O}} = 0$) as a function of pK_a and pK_a^* at equilibrium (a) pH = 0, (b) pH = 7, (c) pH = 14. Bottom Row: 3D plots showing splitting of steady-state quasi-chemical potentials for protons (μ_{H^+}) and hydroxides ($-\mu_{\text{OH}^-}$) as a function of pK_a and pK_a^* at (d) pH = 0, (e) pH = 7, (f) pH = 14. These data were plotted this way in order to mimic depictions of quasi-Fermi levels (qFLs) for mobile charged species electrons ($\text{qFL}_{e^-} = \mu_{e^-}$) and holes ($\text{qFL}_{h^+} = -\mu_{h^+}$) in electronic semiconductors, which often assume that $\mu_{\text{semiconductor}} = \mu_{\text{semiconductor}}^0 = 0$, and thus $\mu_{e^-} = \mu_{h^+} = 0$ at chemical equilibrium.

The largest set of pK_a and pK_a^* combinations that are able to perform significant amounts of useful work occurs when equilibrium pH = 7 (see lower right and upper left corners of **Figure 2b**), due to non-negligible changes in the chemical potential for $\text{H}^+(\text{aq})$ and/or $\text{OH}^-(\text{aq})$, which motivated us to further assess details of these conditions. Half-maximum changes in total protonic chemical potential are possible when $|\Delta pK_a| \approx 8$ and Nernstian changes in total protonic chemical potential are possible when $|\Delta pK_a| \approx 6$, a condition that we define as when the sum of the steady-state chemical potentials for $\text{H}^+(\text{aq})$ and $\text{OH}^-(\text{aq})$ is approximately equal to $(\ln 10)k_B T \approx 5710 \text{ J} (= 59.2 \text{ meV})$. Several common photoacid and photobase motifs exhibit $|\Delta pK_a| \approx 8$, yet non-optimal pK_a and pK_a^* values,^{4,47–53} suggesting that half-maximum changes in total protonic chemical potential may be possible in practice, as long as absolute pK_a and pK_a^* values can be altered, which

should be possible using the tools of synthetic chemistry.⁵² Electronically, this requires that changes in free energy due to alterations in electron density from absorption of a photon significantly influence regions of the dye molecule that are involved in localized proton transfer. Mechanistically, this means that there is a change in the propensity of a functional group to deposit a proton onto $\text{OH}^-(\text{aq})$ or $\text{H}_2\text{O}(\text{l})$, or abstract a proton from $\text{H}^+(\text{aq})$ or $\text{H}_2\text{O}(\text{l})$. Alternatively, photoacids or photobases capable of attaining near-maximum changes in total protonic chemical potential have not been demonstrated, because the magnitude of required changes in free energy are quite large, i.e. $|\Delta pK_a| \approx 12$. One way to overcome this gap in performance is to identify new design strategies beyond the Förster cycle (**Figure 1a**). Examples include concepts that rely on nonradiative processes such as conical intersection curve crossing transitions with significant nuclear motion during excited-state proton transfer and/or considerations of changing the bonding arrangement during excited-state proton transfer to alter the nature of the functional group.

The sum of the steady-state chemical potentials for $\text{H}^+(\text{aq})$ and $\text{OH}^-(\text{aq})$ is useful for predicting sunlight-to-protonic power conversion efficiencies (η) (**Figure 3**). Like outcomes from similar analyses that assumed devices based on electronic semiconductors, chemical potentials and η values are determined by assuming a constant system temperature, even though most of the absorbed photon energy is lost as heat, and with a significant, but lesser, amount transmitted or reemitted. Herein, reasonable efficiency limits are determined as the product of the following three terms, divided by the incident solar irradiance of 100 mW/cm^2 :³³ the rate of generation of excited-state photoacid or photobase species, the change in the total protonic chemical potential, and 0.75 as an approximate fill factor based on these values.⁵⁴ The thermodynamically rigorous change in total protonic chemical potential, in units of eV (**Figure 2b**), is a nomenclature that is independent of the type of work that is performed, and is equal to the value of the open-circuit photovoltage

(V_{oc}), in units of V, when electric work is specifically performed (**Figure 3a**). To complement V_{oc} , kinetically rigorous reaction rates projected as a flux of electric work are reported as short-circuit photocurrent density (J_{sc}) (**Figure 3b**). We define J_{sc} as the product of the Faraday constant, ℓ , and the rate of photon absorption by the desired protonation state of the ground-state dye species in

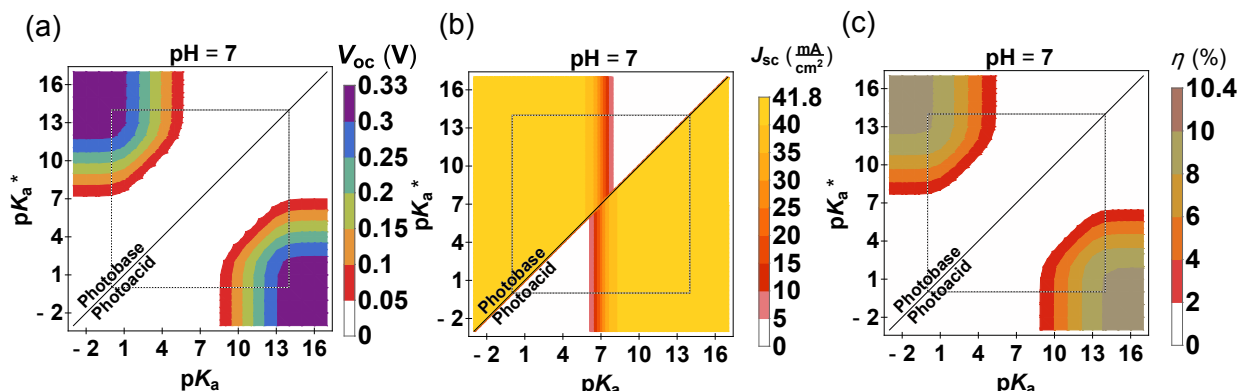


Figure 3. Contour plots of reasonable limits to the (a) open-circuit photovoltage (V_{oc}), by replacing eV with V in **Figure 2b**, (b) short-circuit photocurrent density (J_{sc}), and (c) sunlight-to-protonic power conversion efficiency (η) assuming a fill factor equal to 0.75, as a function of pK_a and pK_a^* at optimal equilibrium pH ($pH = 7$). J_{sc} was calculated based on the rate of photon absorption by the desired protonation state of the ground-state dye species in each half of the two-parameter contour plot, i.e. PAH as photoacids in the lower right and PA^- as photobases in the upper left.

each half of the two-parameter contour plot, i.e. PAH as photoacids in the lower right and PA^- as photobases in the upper left. The rather abrupt change in J_{sc} values near $pK_a \approx 7$ occurs because pH was assumed to be equal to 7, and therefore the percentage of conjugate bases/acids varies significantly at that pK_a value and their absorption is parasitic to photocurrent generation. As such, this definition for J_{sc} is analogous to that used to describe electronic solar photovoltaic devices in the presence of parasitic absorption, e.g. due to intraband absorption by conduction-band electrons and/or valence-band holes.⁵⁵ Combined, these effects suggest that the power output, and therefore η (**Figure 3c**), of sunlight-driven proton pumps based on photoacid or photobase dyes are most influenced by V_{oc} , and thus the sum of the steady-state chemical potentials for $H^+(aq)$ and $OH^-(aq)$. For this reason, our analyses below focus on the influence that thermodynamic and kinetic parameters of the system have on these total protonic chemical potentials as the predominant

performance metric. Moreover, values of η cannot exceed the thermal detailed-balance limit, first derived by Shockley and Queisser,¹¹ but can be increased by processes invoked for use in electronic semiconductor devices, such as solar optical concentration, multiple-exciton generation, singlet fission, upconversion, downconversion.

While the change in the sum of the steady-state chemical potentials for mobile charged species alone is what is needed to predict whether a photochemical system can perform useful work, it is also instructive to examine the chemical potential of each mobile charged species, i.e. $\text{H}^+(\text{aq})$ and $\text{OH}^-(\text{aq})$ herein. By analogy to quasi-Fermi levels (qFLs) in solid-state physics, which in the absence of spatially varying electric potentials are defined as $\text{qFL}_{e^-} = \mu_{e^-}$ and $\text{qFL}_{h^+} = -\mu_{h^+}$, the data in **Figure 2d,e,f** are plotted as μ_{H^+} and $-\mu_{\text{OH}^-}$.⁷ These data suggest that while each representative equilibrium pH condition can exhibit steady-state chemical potentials for mobile charged species that sum to as large as ~ 330 meV, the mobile charged species whose chemical potential dominates the sum depends significantly on equilibrium pH. This observation is consistent with behavior for electronic semiconductors⁵⁵ where doping, by analogy to pH, generates excess mobile charged species of one type at equilibrium, i.e. majority carrier species. Upon absorption of light or application of an electric polarization bias, an equal number of mobile charged species are generated in the system. This most greatly perturbs the concentration of species initially present at low concentration, i.e. minority carrier species, and is consistent with the data in **Figure 2d,e,f**. The equality of this process in water and in electronic semiconductors⁵⁵ further supports that water is a protonic semiconductor.² However, unlike for electronic semiconductors, photoacid and photobase dyes do not simultaneously generate highly mobile charged species of both charge types upon exciton dissociation. Instead, the four sequential steps in the Förster cycle (**Figure 1a**) result in significant generation of one charge type before the other, such that most

noticeably when undoped, i.e. at equilibrium $\text{pH} = 7$, and for strong photoacids or photobases, i.e. $\text{p}K = 0$, the sum of the steady-state chemical potentials for mobile charged species is dominated by one species, i.e. the minority carrier species, at intermediate $\text{p}K_a$ values (**Figure S2**). This behavior underscores the importance of including elementary reaction steps in detailed-balance models for photochemical energy conversion.

Effects of thermodynamic parameters on rates of reactions in the Förster cycle

Near-optimal performance for sunlight-to-protonic energy conversion is possible for a small set of $\text{p}K_a$ and $\text{p}K_a^*$ combinations with extreme values and a rather large $|\Delta\text{p}K_a|$, while near-zero sunlight-to-protonic energy conversion is possible for the majority of the $\text{p}K_a$ and $\text{p}K_a^*$ combinations with mid-range values (**Figures 1 – 3**). Further insight into the cause of this behavior is obtained by analyzing relative rates of the desired and undesired reactions. The four desired reactions that each constitute a step in the Förster cycle are different for photoacids and photobases (**Table 2**). **Figure 4** shows, for optimal equilibrium pH ($\text{pH} = 7$), net rates for each of these desired steps (A, B, C,

Table 2. Reactions of the dye sensitization Förster cycle to affect $\text{H}_2\text{O}(\text{l}) + \text{photon} \rightarrow \text{H}^+(\text{aq}) + \text{OH}^-(\text{aq})$.

Step	Photoacid Reactions	Photobase Reactions	Quantum Yield
A	$\text{PAH} + h\nu_{\text{PAH}} \rightarrow \text{PAH}^*$ (Reaction 7f)	$\text{PA}^- + h\nu_{\text{PA}^-} \rightarrow \text{PA}^{*-}$ (Reaction 8f)	α_A
B	$\text{PAH}^* \rightarrow \text{PA}^{*-} + \text{H}^+$ (Reaction 4f)	$\text{PA}^{*-} + \text{H}_2\text{O} \rightarrow \text{PAH}^* + \text{OH}^-$ (Reaction 5f)	Φ_B
C	$\text{PA}^{*-} \rightarrow \text{PA}^- (+ h\nu_{\text{PA}^-})$ (Reaction 8b)	$\text{PAH}^* \rightarrow \text{PAH} (+ h\nu_{\text{PAH}})$ (Reaction 7b)	Φ_C
D	$\text{PA}^- + \text{H}_2\text{O} \rightarrow \text{PAH} + \text{OH}^-$ (Reaction 3f)	$\text{PAH} \rightarrow \text{PA}^- + \text{H}^+$ (Reaction 2f)	Φ_D

D) in green-scale and net rates for undesired reactions in grey-scale or red-scale. For clarity, and to illustrate the dominant process, only the reaction with the fastest net rate is plotted for any combination of $\text{p}K_a$ and $\text{p}K_a^*$ values, with processes from the Photoacid (Photobase) column in **Table 2** shown in the lower right (upper left) region of **Figure 4**. Near the condition of $\text{p}K_a = \text{p}K_a^*$, net reaction rates approach zero due to competing photoacid and photobase processes. Steady-state

rates for each net reaction (**Reactions 1 – 8**) and their single-direction elementary reaction steps are shown in **Figures S3 and S4**.

Data for Step A (and C) of the Förster cycle shown in **Figure 4a** are symmetric about the

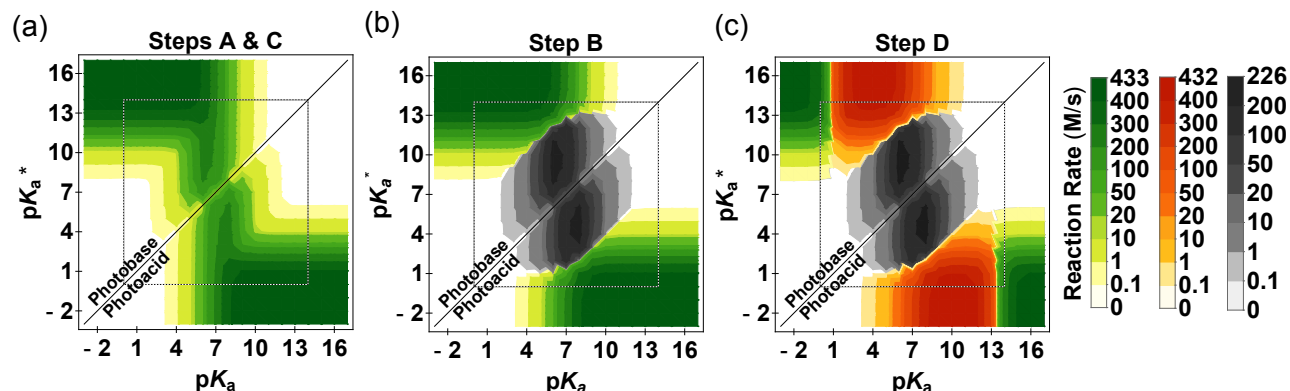


Figure 4. Förster cycle step-centric, rather than reaction-centric, contour plots that succinctly generalize the different reactions that photoacids and photobases can undergo during the Förster cycle. While there is significant overlap in processes (signified by the three color tones), for enhanced clarity, only the dominant process for each combination of pK_a and pK_a^* values is shown at optimal equilibrium pH ($pH = 7$). **Step A** shows in the lower right the net rate of photo-excitation of protonated ground-state (PAH) photoacid (**Reaction 7**) and in the upper left the net rate of photo-excitation of ground-state deprotonated (PA^-) photobase (**Reaction 8**). **Step B** shows in the lower right the net rate of excited-state protonated (PAH*) photoacid ESPT to water (**Reaction 4**, green-scale) and to PA^- (**Reaction 6**, gray-scale), and in the upper left the net rate of excited-state deprotonated (PA^{*-}) photobase ESPT from water (**Reaction 5**, green-scale) and to PAH (**Reaction 6**, gray-scale). **Step C** shows in the *upper left* the net rate of PA^{*-} photoacid recombination to its ground state (**Reaction 8**) and in the *lower right* the net rate of PAH* photobase recombination to its ground state (**Reaction 7**), but because the figure is symmetric about the line where $pK_a = pK_a^*$, the lower right depicts the net rate of PA^{*-} photoacid recombination to its ground state (**Reaction 8**) and the upper left depicts the net rate of PAH* photobase recombination to its ground state (**Reaction 7**). **Step D** shows in the lower right the net rate of proton transfer to PA^- photoacid from water (**Reaction 3**, green-scale), from $H^+(aq)$ (**Reaction 2**, red-scale), and from PAH* (**Reaction 6**, gray-scale), and in the upper left the net rate of proton transfer from PAH photobase to water (**Reaction 2**, green-scale), to $OH^-(aq)$ (**Reaction 3**, red-scale), and to PA^{*-} (**Reaction 6**, gray-scale).

line where $pK_a = pK_a^*$ and indicate that the net rate of sunlight absorption by dye molecules to generate excited-state species results in greater-than-half-maximum reactivity when $pK > 7$ and $pK^* < 2.5$ (**Figure S5**). The reason that dye molecules with $pK < 7$ result in less-than-half-maximum reactivity is because at equilibrium $pH = 7$, greater than half of the ground-state dye molecules are in the incorrect protonation state to perform ESPT, and thus sunlight absorption by species in the incorrect protonation state dominates. The reason that dye molecules with $pK^* > 2.5$

result in less-than-half-maximum reactivity is not due to poor sunlight absorption, but rather non-unity quantum yields for ESPT (Step B) (**Figure 5a,c**), which means that some of the excited-state species return to their ground states without undergoing any photochemical reactions (**Figures S3 and S4**). These results differ substantially from those obtained from prior thermal detailed-balance models of general photovoltaic and photochemical systems,^{11,12} where an external load that approaches zero resistance can be present and therefore photon absorption alone can result in useful power generation. Instead, our observations are reminiscent of detailed-balance models that include a chemical load,^{15,16,56} where a significant change in chemical potential is required for at least some photogenerated mobile charged species to perform net chemical reactions, like the conditions resulting in green-scale zones in **Figure 4a**, while other conditions result in substantially less net reactivity, for example, when $pK^* > 2.5$.

The fact that the green-scale zones in **Figure 4a** encompass a significantly larger set of pK_a and pK_a^* combinations than the colored regions in **Figure 2b** suggests that having net rates for sunlight absorption to generate excited-state species does not guarantee that ESPT will result in changes in chemical potential, and therefore changes in concentrations, of $H^+(aq)$ and $OH^-(aq)$. This is evident based on comparisons of net rates observed for Step B of the Förster cycle (**Figure 4b**) versus Step A (**Figure 4a**). Differences in these data are due to ESPT self-quenching of excited-state dyes by ground-state dyes, which occurs in part because of the large value of c_{total} (= 1 M) used in the base-case model. Decreasing c_{total} decreases the rate of this dye self-quenching process until it is negligible, which is shown below. The similarity in the coloration of the green-scale zones in **Figure 4a,b** suggests that the quantum yield for ESPT to form a desired reaction product, and not dye self-quenching, is near unity for most combinations of pK_a and pK_a^* values that result in greater-than-half-maximum reactivity (**Figures 5a,c and S5**). Net rates for Step C of

the Förster cycle, which represents recombination from the other protonation state of the excited-state dye, meaning the deprotonated conjugate base for photoacids and the protonated conjugate acid for photobases, are equal to the rates shown in **Figure 4a** and, by definition, exhibit unity quantum yield.

Subsequent to net sunlight absorption (Step A), major causes for inefficiencies are the various reactions that are possible to regenerate ground-state dyes after ESPT, which is the final Step D of the Förster cycle (**Figures 4c and 5b,d**). In this step, over half of the set of pK_a and pK_a^* combinations where ESPT successfully forms desired mobile charged species of H^+ , from excited-

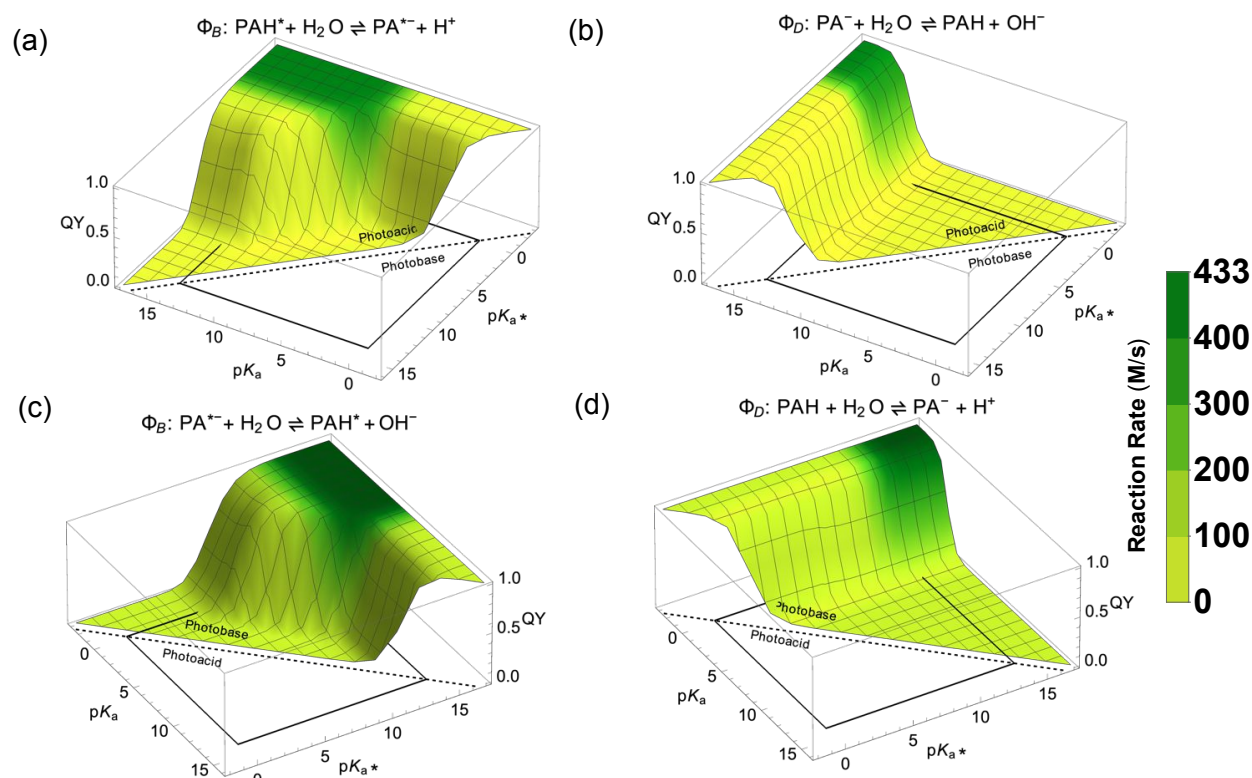


Figure 5. Reaction-centric contour plots at optimal equilibrium pH ($pH = 7$) showing quantum yields (heights) and steady-state net reaction rate (colors) for the thermal reactions that photoacid species (top row) and photobase species (bottom row) undergo during the idealized Förster cycle: (a) **Step B, Reaction 4**, (b) **Step D, Reaction 3**, (c) **Step B, Reaction 5**, (d) **Step D, Reaction 2**.

state photoacids, or OH^- , from excited-state photobases, (**Figure 4b**) consume the photogenerated mobile charged species during regeneration (Step D). While this mechanism results in a nonzero steady-state chemical potential for at least one mobile charged species, their sum is far from

maximum (**Figure 2b** (non-purple colored regions) and **Figures S3 and S4, Reactions 2 and 3**). The rationale for these various mechanisms, and the resulting significantly smaller green-scale zones in **Figure 4c** in comparison to **Figure 4a,b**, are due to the driving-force dependence to the rate constant for proton transfer to and from H^+ , OH^- , and water. Only for $\text{p}K > 13.5$ can deprotonation of water by deprotonated ground-state photoacids (**Reaction 3f**) or protonation of water by protonated ground-state photobases (**Reaction 2f**) outcompete proton transfer from H^+ (**Reaction 2b**) or to OH^- (**Reaction 3b**), respectively. Overall the set of $\text{p}K_{\text{a}}$ and $\text{p}K_{\text{a}}^*$ combinations encompassed by the green-scale zones in **Figure 4c** equals that encompassed by the colored regions in **Figure 2b**, indicating substantial formation of desired reaction products of H^+ and OH^- and therefore net heterolytic water dissociation.

The steady-state net volumetric rate of light-driven heterolytic water dissociation and water formation can be recast as a product of the incident photon fluence rate and the quantum yields for each intermediate step as follows,

$$\text{Rate}_{\text{total,ss}} = (I_{\text{solar}_0}/\ell) \times \alpha_{\text{A}} \times \Phi_{\text{B}} \times \Phi_{\text{C}} \times \Phi_{\text{D}} \quad (14)$$

where α_{A} is the desired absorbance due to photoacid or photobase species, with a value in the range of [0, 1], and each Φ_i is a net quantum yield for reaction step, i , with a value in the range of [0, 1]. The product of I_{solar_0} , α_{A} , and the Faraday constant is equal to the current density as depicted in **Figure 3b**, by definition $\Phi_{\text{C}} = 1$, and the remaining quantum yields, Φ_{B} and Φ_{D} , are calculated by dividing the net reaction rate for each step by the net reaction rate for the previous step. The overlapping regions of maximum quantum yields (**Figure 5**) and maximum net reaction rates (**Figures 5, S3, and S4**) for Steps B and D of the Förster cycle coincide perfectly with the green-scale zones in **Figure 4b,c**. These data also indicate that the quantum yield remains large even

when the net reaction rate slows; for Step B this occurs as pK values decrease concomitant with increases in parasitic sunlight absorption, and for Step D this occurs as pK^* values increase concomitant with decreases in the net rate of ESPT.

Simulations performed using the base-case model provide important insights into expected outcomes of photochemical energy conversion using photoacids or photobases. However, the base-case model includes several simplifications whose accuracy could be improved. For example, empirically it has been shown that when pK_a values lie outside of the protonic water window range of $[0, 14]$, rate constants for proton transfer with water increase,⁵⁷ but not by an order-of-magnitude per pK_a value as expected for a Brønsted slope equal to one, requiring that reverse second-order rate constants concomitantly decrease, but by a lesser amount. To simulate the limit of this behavior, for the base-case model at equilibrium $pH = 7$ we switched values for the Brønsted slopes of pK_a as a function of thermodynamic driving force when the values were outside of the water window range. Notwithstanding, total protonic chemical potentials were nearly indistinguishable from those obtained for the base-case model (**Figure S6a**). In addition, while proton-transfer reactions for simple Brønsted–Lowry acids and bases follow Brønsted relations, which is assumed for all proton-transfer reactions in the base-case model, more complex acids and bases, including photoacids and photobases, do not. Instead, they exhibit nonzero values of ΔG^\ddagger , even for some isoergic/exoergic reactions, with behavior that is consistent with the Marcus normal region, resulting from BEBO considerations in Marcus theory.^{19–21} Notwithstanding, simulations performed using the base-case model at equilibrium $pH = 7$ modified to include effects of Marcus BEBO theory, using empirically determined values for ΔG^\ddagger when $\Delta G^0 = 0$,^{19–21} resulted in smaller rate constants for bimolecular proton-transfer reactions, yet total protonic chemical potentials that were nearly indistinguishable from those obtained for the base-case model (**Figure S6b**).

Moreover, electric fields have been shown to significantly increase rate constants for thermodynamically unfavorable charge-forming proton-transfer reactions,^{31,32} like heterolytic water dissociation,^{30–32} i.e. $k_{1,\text{dl}}$, and therefore $K_{1,\text{w}}$. Simulations performed using the base-case model at equilibrium pH = 7 with this exponential electric-field enhancement resulted in total protonic chemical potentials that decreased by a Nernstian shift of ~ 59.2 meV per order-of-magnitude increase in rate constants in comparison to those obtained for the base-case model (**Figure S7**). This behavior is expected because it is analogous to increasing, at thermal equilibrium, the rate of generation and recombination of mobile charged species electrons and holes in an electronic semiconductor, which underscores that this outcome is independent of whether rate constants are enhanced due to an electric field or another process. This often occurs in practice due to nonradiative processes that decrease V_{oc} values in a Nernstian fashion per order-of-magnitude decrease in the photoluminescence quantum yield, due to the same factor increase in the observed rate constant for excited-state recombination. Lastly, like earlier works by Shockley, Queisser, Ross, Hsiao, Bolton, et al., we considered all thermodynamic and kinetic parameters, and species concentrations, to be spatially homogeneous. This is a reasonable assumption in our model because each population of excited-state species will approximately homogenize over our chosen optical pathlength of 10 nm. In practice, larger optical pathlengths will likely negatively influence performance due to transport limitations.

Many of the aforementioned considerations were driven by experimental observations and not rigorous first principles. However, this is not true for detailed balance, which is a fundamental physical principle that is rooted in several other fundamental physical principles and laws, i.e. the principle of microscopic reversibility, the law of mass action, the law of mass conservation, Hess's law. Thermal detailed balance is a cornerstone of models reported by Shockley, Queisser, Ross,

Hsiao, Bolton, et al., and while the base-case model herein uniquely included rigorous chemical detailed balance, it excluded thermal detailed balance due to its perceived limited impact on simulation results and increased clarity of data interpretation. Nevertheless, to verify these presumptions we evaluated the impact of combined chemical and thermal detailed-balance conditions for the base-case model at equilibrium $\text{pH} = 7$. With knowledge of the equal temperature of the system and the surroundings, and wavelength-dependent values of the absorption coefficient, we calculated the radiative (minimum) rate constants for generation and recombination of excited-state species (**Figure S8**), as well as the equilibrium concentration of all excited-state species, thus allowing mass-action expressions for those processes to be included in the model. Using the experimentally validated approximate Strickler and Berg analysis⁵⁸ and a physically plausible Gaussian absorption spectral lineshape for the dyes (**Figure S9a**), the following conditions for the base-case model were replicated: total sunlight absorption, maximum absorption coefficient, and excited-state lifetime for photoacids and photobases of 5 ns that was entirely radiative, as the reciprocal of the approximate value of the Einstein A coefficient first-order rate constant. Simulation results indicate that the rate of radiative generation and recombination of the excited state of the conjugate base or acid in the absence of solar radiation is at least 5 orders-of-magnitude slower than the rate of sunlight absorption by photoacids or photobases, respectively, in the presence of solar radiation. As such, and as originally presumed, changes in total protonic chemical potential are nearly indistinguishable from those obtained for the base-case model where thermal detailed balance was not included (**Figure S10a,b**). One outcome of the combined thermal and chemical detailed-balance model is the discovery that a unity photoluminescence quantum yield for a photoacid or photobase results in a non-unity photoluminescence quantum yield, and a bathochromic-shifted photoluminescence spectrum, for

the excited state of its conjugate base or acid, respectively (**Table S2**). Moreover, thermal detailed balance defines equilibrium concentrations of excited-state species, and thus allows their chemical potentials to be determined when the system is perturbed due to absorption of sunlight. Results indicate that larger changes in chemical potential occur for the excited state of photoacids and photobases than protonic water species (**Figure S10c-f**), which is expected because the former subsequently generate the latter.

Effects of excited-state lifetimes on sunlight-to-protonic photochemical energy conversion

In standard models used to calculate detailed-balance power conversion efficiencies in the radiative limit,^{11,12,15,16} observed excited-state lifetime is inherent based on the rate of generation of excited-state species, which is affected by ambient temperature, refractive indices, absorption coefficients, photon or electron multiplication or removal processes, photoluminescence quantum yield, and optical pathlength, where observed excited-state lifetime increases when thicker materials are used due to more photon recycling events.⁵⁹ Therefore, previous models that varied any of these parameters in order to determine their influence on performance, also implicitly varied observed excited-state lifetime. For this reason, excited-state lifetimes used in the base-case model ($\tau_{7,\text{PAH}^*} = \tau_{8,\text{PA}^-} = 5$ ns), which are values that are representative of actual photoacids and photobases,^{36–38} are kinetic parameters that influence steady-state chemical potentials for $\text{H}^+(\text{aq})$ and/or $\text{OH}^-(\text{aq})$. Although a complete suite of data that expands the three-parameter ($\text{p}K_{\text{a}}$, $\text{p}K_{\text{a}}^*$, equilibrium pH) contour plots (**Figure 1b**) to four parameters ($\text{p}K_{\text{a}}$, $\text{p}K_{\text{a}}^*$, equilibrium pH, τ) would be insightful, results would be difficult to interpret. Therefore, we chose equilibrium pH = 0, pH = 7, and pH = 14 and varied τ_{7,PAH^*} ($= \tau_{8,\text{PA}^-}$) as three-parameter, three-dimensional contour plots

(Figure S11). To provide further insight, and because the general shapes of the contours in regions of greater-than-Nernstian total protonic chemical potential are unaffected by choice of parameter values, Pareto fronts representing Nernstian total protonic chemical potential are reported for

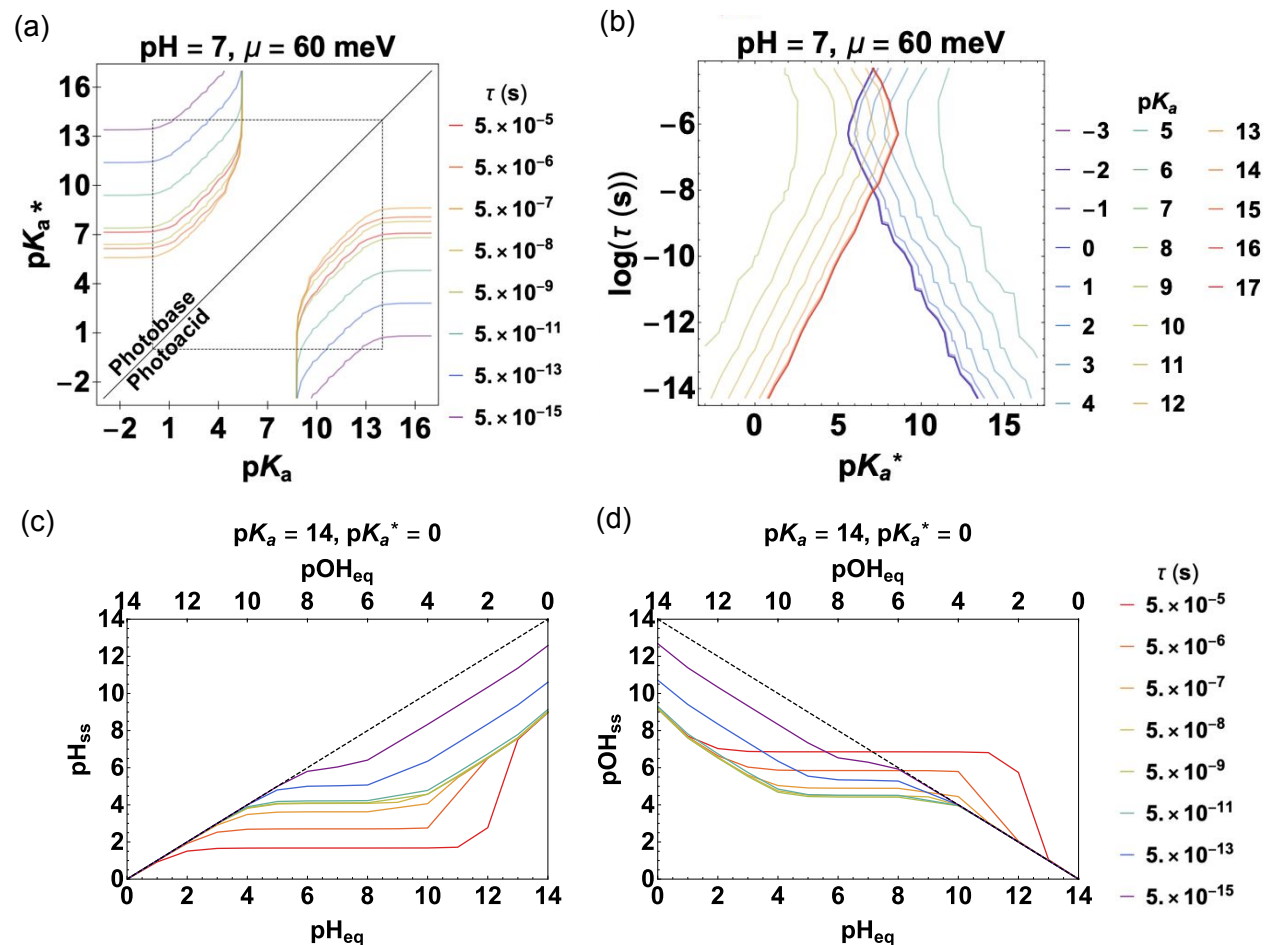


Figure 6. (a,b) Pareto fronts for Nernstian total protonic quasi-chemical potential ($\mu = \mu_{H^+} + \mu_{OH^-} = 60$ meV) at optimal equilibrium pH ($\text{pH} = 7$) and with base-case total dye concentration ($c_{\text{total}} = 1$ M) shown as two different two-parameter plots: (a) $\text{p}K_a$ and $\text{p}K_a^*$ for the series of excited-state lifetimes ($\tau = \tau_{7,PAH} = \tau_{8,PA^*}$), (b) $\text{p}K_a^*$ and τ for the series of $\text{p}K_a$. (c,d) Steady-state (ss) (c) pH and (d) pOH for optimal photoacids ($\text{p}K_a = 14$, $\text{p}K_a^* = 0$), each as a function of equilibrium (eq) pH (bottom axis) and pOH (top axis) for the series of τ , and including equilibrium data (black dashed line).

optimal equilibrium pH ($\text{pH} = 7$) as three-parameter, two-dimensional plots as ($\text{p}K_a$, $\text{p}K_a^*$ for a series of τ) (Figure 6a) and ($\text{p}K_a^*$, τ for a series of $\text{p}K_a$) (Figure 6b). (Additional plots showing other combinations of parameters are reported as Figures S12 – S14.) These data show that as τ decreases, the range of $\text{p}K_a^*$ values in the zones encompassed by the Pareto fronts decreases, while

the range of pK_a values changes little, which is expected because τ is an excited-state parameter. Smaller values of τ mean that dyes exist in their excited states for less time, providing fewer opportunities for ESPT (and dye self-quenching), and therefore only dyes with large rate constants for ESPT, meaning small values of pK^* , exhibit large values of Φ_B . Conversely, larger values of τ enable dyes with small rate constants for ESPT, meaning large values of pK^* , to exhibit large values of Φ_B . But this trend only persists until $\tau \approx 1 \mu\text{s}$, after which the range of pK^* values in the zones encompassed by the Pareto fronts decreases as is apparent from the data shown in **Figure 6b**, which exhibit non-monotonic linear trends with slopes approximately equal to ± 1 .

The cause of this behavior is clear when considering photoacids with optimal values of $pK_a = 14$ and $pK_a^* = 0$ and examining the resulting steady-state concentrations of H^+ (pH_{ss}) and OH^- (pOH_{ss}) as a function of equilibrated pH and pOH for a series of τ (**Figure 6c,d**). (Analogous data for photobases with optimal values of $pK_a = 0$ and $pK_a^* = 14$ are shown in **Figure S15**.) Unlike the data reported in **Figure 2d,e,f** for $\tau = 5 \text{ ns}$, when $\tau > \sim 1 \mu\text{s}$ the steady-state concentration of OH^- is actually smaller than the equilibrium concentration (**Figures 6d and S16**). This reverse photovoltaic effect occurs because the generation rate of these long-lived excited states allows Step B to occur many times, resulting in a significant change in the concentration of H^+ from excited-state photoacids (OH^- from excited-state photobases), so much so that H^+ (OH^-) recombines with OH^- (H^+) that are part of the equilibrium concentration at a faster rate than they are generated via Step D. As such, results from this equilibrium pH ($= \text{pOH}$) = 7 condition are more indicative of equilibrium pH (pOH) $\ll 7$ conditions, where the range of pK_a^* values in the zones encompassed by the Pareto fronts decreases (**Figure 6a**). Results using even larger values of τ are not reported because in that case, $>10\%$ of the dyes could be in their excited states at steady state, thus requiring consideration of effects due to stimulated emission and/or population

inversion that were not included in the model. Collectively, these analyses and their outcomes, and those below based on variable concentration, were specific for optimal equilibrium pH (pH = 7) or optimal dye thermodynamic parameters ($pK = 14$ and $pK^* = 0$). These conditions were chosen because they represent the best opportunity for efficient sunlight-to-protonic energy conversion, and thus provide upper limits to performance based on other dye parameters, such as excited-state lifetimes and species concentrations.

Analogous to prior thermal detailed-balance models, herein each protonation state of the dye was envisioned to have two electronic states. However, when rigorous thermal detailed-balance conditions are invoked this renders many of the larger τ values simulated in **Figure 6** unphysical. Strickler and Berg analysis under thermal detailed balance and in the radiative limit resulted in $\tau = 5$ ns for photoacids (τ_{7,PAH^*}) or photobases ($\tau_{8,PA^{-*}}$), which are conditions assumed in the base-case model, however the analysis also resulted in $\tau \geq 5$ ns for excited states of their conjugate bases or acids, respectively (**Table S2**). This suggests that $\tau_{7,PAH^*} \neq \tau_{8,PA^{-*}}$, which differs from the assumption that $\tau_{7,PAH^*} = \tau_{8,PA^{-*}}$ used in all models simulated herein. Discrepancies between simulated and theoretical values of τ were remedied by assuming that nonradiative recombination pathways exist for excited states of the conjugate bases or acids, enabling $\tau_{7,PAH^*} = \tau_{8,PA^{-*}}$, and including additional lower-energy optically-dark electronic excited states, such that τ can greatly exceed 5 ns. In total, by expanding the Förster cycle to include two additional optically-dark excited states, one for each of the protonated and deprotonated forms of each dye molecule (**Figure S17**), and assuming they are lower in standard free energy than the original excited states, accessed quickly via intersystem crossing, and exceptionally long-lived, such as optically-dark triplet states, simulation results shown in **Figure 6** are physically possible. The only caveat is that when both $|\Delta pK_a|$ and τ are large, the value of E_{00} for the singlet state of the conjugate base or acid

is so small that the necessary energy reduction of its optically-dark excited state to achieve such large values of τ may render its energy below that of the electronic ground-state singlet.

Effects of total dye concentration on sunlight-to-protonic photochemical energy conversion

Species concentration and absorbance are not often considered in models used to calculate thermal detailed-balance power conversion efficiency limits for electronic semiconductors, because this information is not needed to come to the typical conclusion that absorbed photon fluence rate is linearly related to photocurrent and exponentially related to photovoltage,^{11,12,15,16,56} assuming zero photon recycling.⁶⁰ However, in reaction-specific molecular models, like the one used herein, total dye concentration influences both the rate of photon absorption through modulation of absorbance due to the Beer–Lambert law and the rate of reactivity due to the law of mass action. To decouple these effects, we performed two sets of chemical detailed-balance simulations using a model with realistic conditions (actual absorbance), where changes in total dye concentration affect both absorbance through the Beer–Lambert law and reaction rates through the law of mass action, and a model with hypothetical conditions (fixed absorbance), where absorbance is unaffected by changes in total dye concentration and total dye concentration only affects reaction rates through the law of mass action. The latter model, with so-called hypothetical conditions, is meant to decouple effects of light absorption from reactivity and is not meant to be physical, although it could be achieved in practice using dyes with increased absorption coefficients to compensate for decreased total dye concentration. In which case, implementation of rigorous thermal detailed-balance conditions necessitates inclusion of optically-dark electronic excited states in practice, so that τ can remain constant; for so-called realistic conditions, no additional considerations are necessary.

Although a complete suite of data that expands the three-parameter (pK_a , pK_a^* , equilibrium pH) contour plots (**Figure 1b**) to four parameters (pK_a , pK_a^* , equilibrium pH, c_{total}) would be insightful, results would be difficult to interpret. Therefore, as in the above lifetime analyses, we chose equilibrium pH = 0, pH = 7, and pH = 14 and varied c_{total} , while maintaining a constant $Abs_{total} = 1$, as three-parameter, three-dimensional contour plots (**Figure S18**). To provide further insight, Pareto fronts representing Nernstian total protonic chemical potential are reported for optimal equilibrium pH (pH = 7) as three-parameter, two-dimensional plots as (pK_a , pK_a^* for a series of c_{total}) (**Figure 7a**) and (pK_a , c_{total} for a series of pK_a^*) (**Figure 7b**). (Additional plots showing other combinations of parameters are reported as **Figures S19 – S24**.) These data show that as c_{total} decreases, the range of pK_a^* values in the zones encompassed by the Pareto fronts changes little, which is expected because fixing $Abs_{total} = 1$ means that generation rate is unaffected by changes in c_{total} . Interestingly, however, is that as c_{total} decreases, the range of pK_a values in the zones encompassed by the Pareto fronts increases, so much so that when $c_{total} = 1$ mM the Pareto front includes pK values as small as ~ 6 . This outcome is unexpected because for $pK \approx 6$, and equilibrium pH = pOH = 7, only $\sim 10\%$ of the ground-state dyes are in the correct protonation state to perform ESPT, which seemingly should negatively influence performance, even when Abs_{total} remains fixed. Notwithstanding, similar to the data shown in **Figure 6b**, the data shown in **Figure 7b** exhibit linear trends with slopes approximately equal to ± 1 . Results using even smaller values of c_{total} are not reported because in that case, and assuming $Abs_{total} = 1$, $>10\%$ of the dyes could be in their excited states at steady state, thus requiring consideration of effects due to stimulated emission and/or population inversion that were not included in the model.

To explain the cause of the aforementioned unexpected behavior, a suite of steady-state observables are shown for photoacids ($pK_a^* = 0$) in **Figure 8** and photobases ($pK_a^* = 14$) in **Figure**

S25, at the extremes of c_{total} evaluated, 1 mM and 1 M: (a,b) net reaction rates, (c,d) single-direction

elementary reaction rates, (e,f) steady-state concentrations, and (g,h) rate constants. These data

illustrate the complexity in Förster cycle processes where different mechanisms dominate in each

of six regions, listed here for the *photoacidic* condition (**Figure 8**) in order of increasing pK_a value:

(i, ii) $0 < pK_a < 7$ (most photoacids *cannot* perform ESPT), with (i) $\mu_{H^+} + \mu_{OH^-} = 0$, (ii) μ_{H^+}

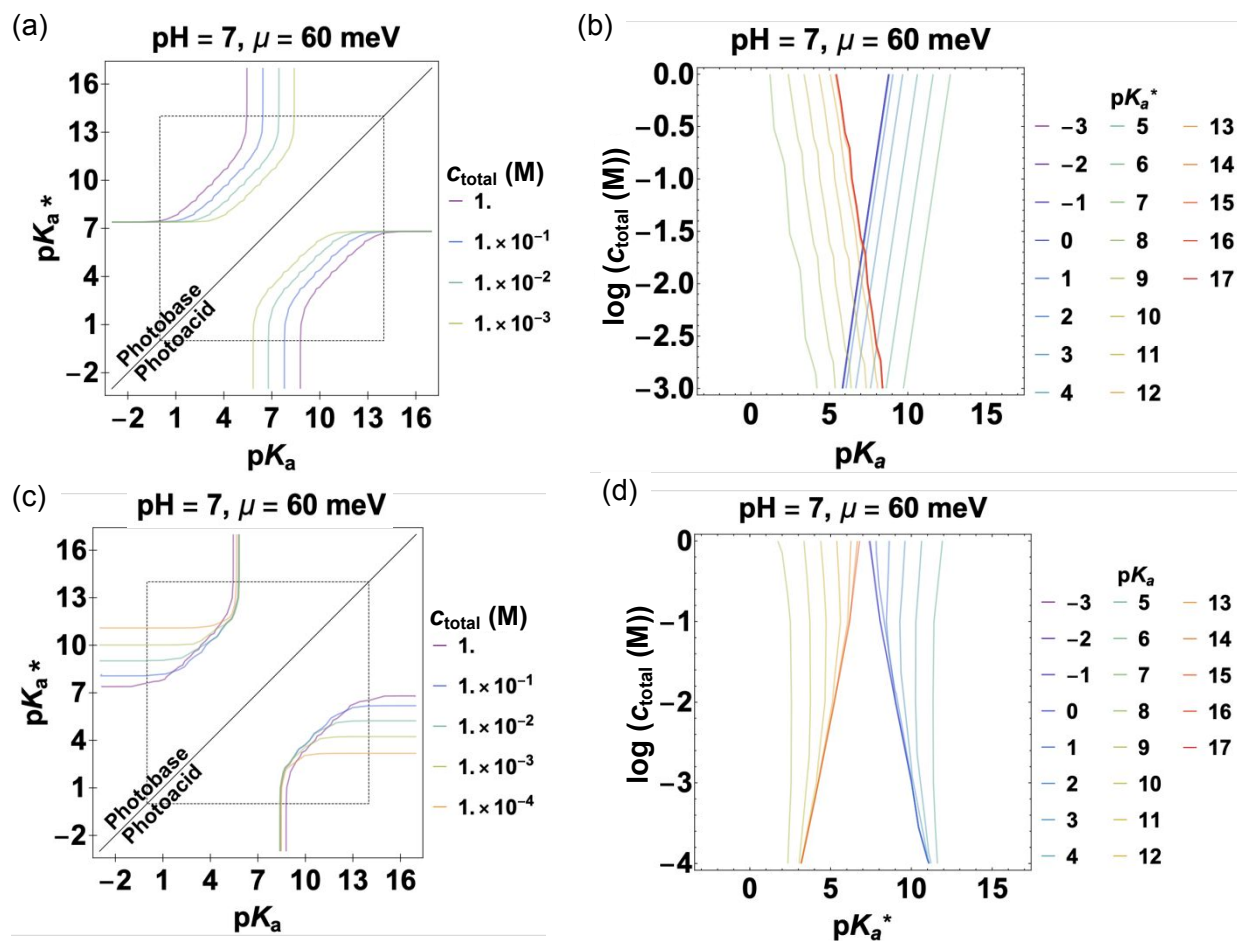


Figure 7. Pareto fronts for Nernstian total protonic quasi-chemical potential ($\mu = \mu_{H^+} + \mu_{OH^-} = 60$ meV) at optimal equilibrium pH ($pH = 7$) and with base-case excited-state lifetimes ($\tau_{7,PAH^*} = \tau_{8,PA^*} = 5$ ns) for the case of fixed absorbance ($Abs_{total} = 1$, top row) and actual absorbance (bottom row) each shown as two different two-parameter plots: (a,c) pK_a and pK_a^* for the series of total dye concentrations (c_{total}), (b) pK_a and c_{total} for the series of pK_a^* , (d) pK_a^* and c_{total} for the series of pK_a .

increasing; (iii, iv, v, vi) $7 < \text{p}K_{\text{a}} < 14$ (most photoacids *can* perform ESPT), with (iii) μ_{H^+}

increasing, (iv) μ_{OH^-} increasing, (v) μ_{OH^-} increasing and μ_{H^+} decreasing, and (vi) μ_{H^+} and μ_{OH^-} unchanging and that sum to their maximum value. (The six regions for the *photobasic* condition

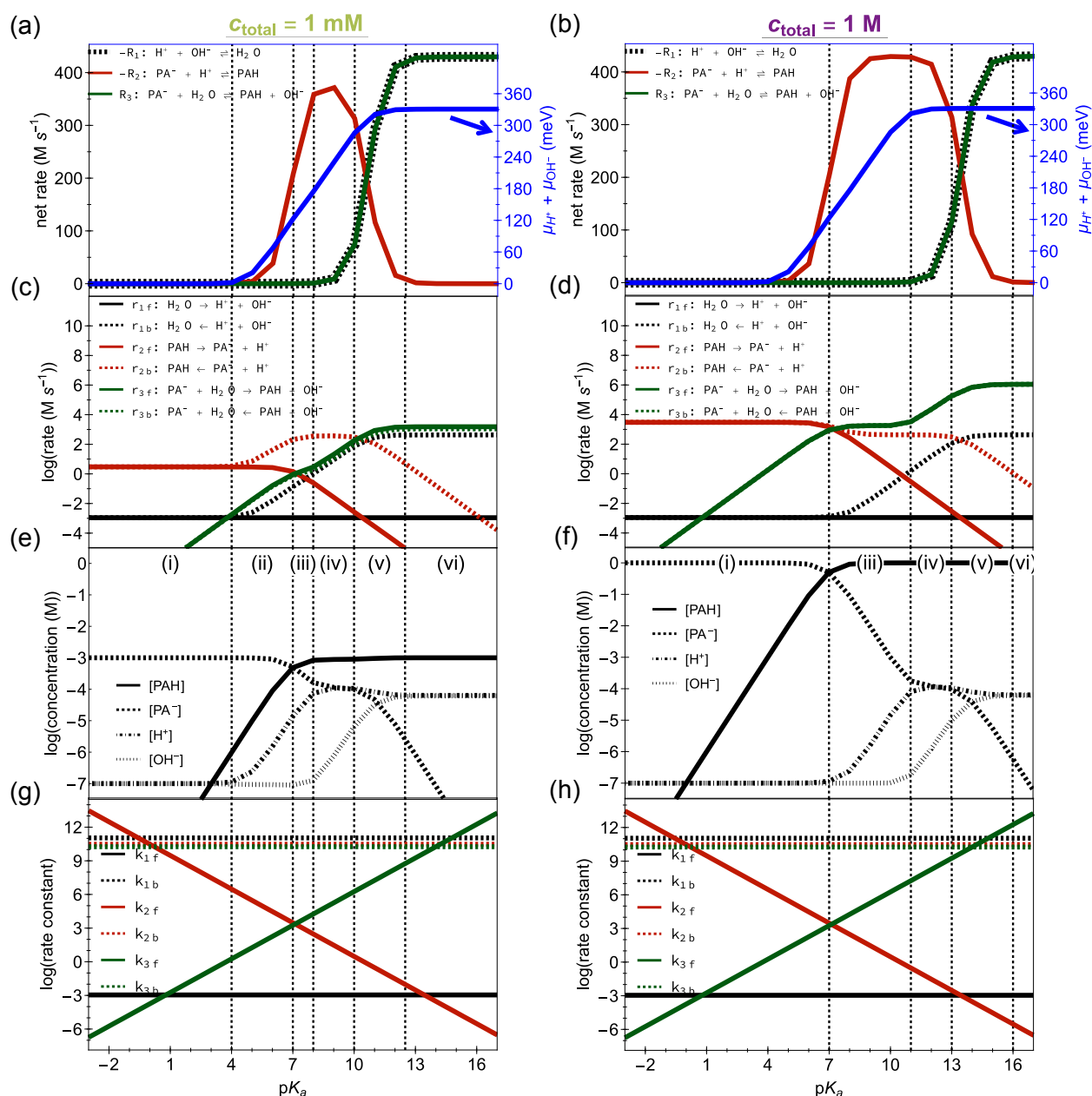


Figure 8. (a,b) Net reaction rates (R_i), (c,d) single-direction elementary reaction step rates (r_i), (e,f) steady-state concentrations, and (g,h) rate constants (k_i) for reaction i , as a function of $\text{p}K_a$ for the two extremes of c_{total} evaluated: 1 mM (left column) and 1 M (right column), at optimal equilibrium pH ($\text{pH} = 7$), optimal photoacid excited-state thermodynamics ($\text{p}K_a^* = 0$), base-case excited-state lifetimes ($\tau_{7,\text{PAH}^*} = \tau_{8,\text{PA}^*} = 5$ ns), and for the case of fixed absorbance ($\text{Abs}_{\text{total}} = 1$), with accompanying data in **Figure 7a,b**. Units for rate constants are not indicated, because they differ for some of the reactions, and region (ii) is intentionally not shown in the right column because it does not exist.

(**Figure S25**) in order of decreasing $\text{p}K_a$ value are (i, ii) $7 < \text{p}K_a < 14$ (most photobases *cannot*

perform ESPT), with (i) $\mu_{\text{H}^+} + \mu_{\text{OH}^-} = 0$, (ii) μ_{OH^-} increasing; (iii, iv, v, vi) $0 < \text{p}K_{\text{a}} < 7$ (most photobases *can* perform ESPT), with (iii) μ_{OH^-} increasing, (iv) μ_{H^+} increasing, (v) μ_{H^+} increasing and μ_{OH^-} decreasing, and (vi) μ_{H^+} and μ_{OH^-} unchanging and that sum to their maximum value.)

In regions (i) and (ii), equilibrium $\text{pH} > \text{p}K_{\text{a}}$ and therefore, based on the Henderson–Hasselbalch equation (**Equation 13**), greater than half of the ground-state photoacid dyes are in the incorrect protonation state to perform ESPT, i.e. PA^- . This results in a less-than-optimal rate of light absorption (Step A), and a concomitant decrease in the steady-state net rate of all subsequent steps in the Förster cycle, which decrease as $\text{p}K_{\text{a}}$ decreases, thus rationalizing the trends in μ_{H^+} . However, for $c_{\text{total}} = 1 \text{ M}$, equilibrium $\text{pH} = 7$, and a modest $\text{p}K_{\text{a}}$ value (≈ 5), $[\text{PAH}]_{\text{eq}} \approx 0.01 \text{ M}$ and thus it might be expected that $[\text{H}^+]_{\text{ss}} \gg [\text{H}^+]_{\text{eq}} (= 10^{-7} \text{ M})$ and $\mu_{\text{H}^+} > 0$. However, this is not observed because of the rapid rate of ground-state reactions at chemical equilibrium, i.e. generation of H^+ from PAH and recombination of H^+ to PA^- (**Reaction 2**). This microscopically reversible rate at chemical equilibrium equals $\sim 10^3 \text{ M/s}$, as the product of $[\text{PA}^-]_{\text{eq}} (\sim 0.99 \text{ M})$, $[\text{H}^+]_{\text{eq}} (10^{-7} \text{ M})$, and the diffusion-limited rate constant, $k_{2b} (\sim 10^{10} \text{ M}^{-1} \text{ s}^{-1})$, which is more than two times faster than the maximum possible rate of photogeneration of H^+ via Step A in the Förster cycle, which is $\sim 4.3 \times 10^2 \text{ M/s}$ and is scaled by the absorptance of dyes in the correct protonation state to perform ESPT. The significantly faster reaction rates at chemical equilibrium result in $\mu_{\text{H}^+} \approx 0$, which would also occur in a highly inefficient solar cell whose large reverse saturation current density measured in the absence of solar irradiation would generate electron–hole pairs at a rate that is faster than they are photogenerated under solar irradiation, resulting in a negligible value for V_{oc} . In our model, at $c_{\text{total}} = 1 \text{ M}$ this effect is so dramatic that region (ii), where $\mu_{\text{H}^+} > 0$, is nonexistent.

The trends in regions (i) and (ii) differs substantially from those in region (iii), because in region (iii) equilibrium $\text{pH} < \text{p}K_a$ and therefore, based on the Henderson–Hasselbalch equation (**Equation 13**), greater than half of the ground-state photoacid dyes are in the correct protonation state to perform ESPT, i.e. PAH. This means that $[\text{PAH}]_{\text{eq}}$ is near- $\text{p}K_a$ -independent and thus that the rate of Step A in the Förster cycle, and all subsequent steps, are near- $\text{p}K_a$ -independent and occur at the same steady-state net rate. Because of the small rate constant for reprotonation by H_2O , k_{3f} , (**Reaction 3f**) regeneration of PAH (Step D) occurs nearly exclusively via reprotonation of PA^- with H^+ (**Reaction 2b**). Therefore, to obtain a near- $\text{p}K_a$ -independent rate of regeneration, the product of k_{2b} , $[\text{PA}^-]_{\text{ss}}$, and $[\text{H}^+]_{\text{ss}}$ must be near-constant. The rate constant, k_{2b} , is independent of $\text{p}K_a$ and $[\text{PA}^-]_{\text{ss}} \approx [\text{PA}^-]_{\text{eq}}$, especially when $c_{\text{total}} = 1 \text{ M}$, because in this region $[\text{PA}^-]_{\text{eq}} \gg [\text{H}^+]_{\text{ss}}$. Because $[\text{PA}^-]_{\text{eq}}$, and thus $[\text{PA}^-]_{\text{ss}}$, decrease exponentially as $\text{p}K_a$ increases based on the Henderson–Hasselbalch equation (**Equation 13**), to maintain a near- $\text{p}K_a$ -independent steady-state net rate, $[\text{H}^+]_{\text{ss}}$ must increase exponentially to offset the decrease in $[\text{PA}^-]_{\text{ss}}$. This means that μ_{H^+} increases linearly over this region, a trend that persists until $\text{p}K_a \approx 8$ for the smallest c_{total} examined (1 mM) and $\text{p}K_a \approx 11$ for the largest c_{total} examined (1 M), where $[\text{PA}^-]_{\text{ss}}$ ceases to decrease.

In region (iv), $[\text{PAH}]_{\text{eq}}$ is still near- $\text{p}K_a$ -independent, meaning that the rate of Step A in the Förster cycle, and all subsequent steps, are near- $\text{p}K_a$ -independent and occur at the same steady-state net rate. In addition, $[\text{PA}^-]_{\text{eq}}$ still decreases exponentially, however $[\text{PA}^-]_{\text{ss}}$ transitions to near-constant because as $\text{p}K_a$ increases, k_{3f} increases, and therefore reprotonation of PA^- by H_2O (**Reaction 3f**) starts to contribute significantly to regeneration of PAH (Step D). This results in a transition where the product of k_{3f} and $[\text{PA}^-]_{\text{ss}}$ becomes larger than the near-constant rate for reprotonation by H^+ (**Reaction 2b**), such that $[\text{OH}^-]_{\text{ss}}$, and thus μ_{OH^-} , increase. This increases the

back reaction rate and therefore, to maintain a constant steady-state net rate for Step D, $[\text{PA}^-]_{\text{ss}}$ must remain near constant, because k_{3f} increases exponentially with $\text{p}K_{\text{a}}$.

Region (v) exhibits similar trends as region (iii) in terms of $[\text{PAH}]_{\text{eq}}$ being near- $\text{p}K_{\text{a}}$ -independent and $[\text{PA}^-]_{\text{ss}}$ decreasing exponentially with increasing $\text{p}K_{\text{a}}$, and similar trends as region (iv) in terms of $[\text{OH}^-]_{\text{ss}}$ increasing with increasing $\text{p}K_{\text{a}}$. In addition, as $[\text{OH}^-]_{\text{ss}}$ approaches $[\text{H}^+]_{\text{ss}}$, the steady-state condition is limited by recombination of H^+ and OH^- (**Reaction 1b**), which has a larger rate constant than the rate constant for recombination of H^+ with PA^- such that $[\text{H}^+]_{\text{ss}}$, and thus μ_{H^+} , actually decrease.

In region (vi), the sum of the steady-state chemical potentials for H^+ and OH^- equals its maximum value dictated by when the rate of absorption (Step A) equals the net rate of recombination of H^+ and OH^- (**Reaction 1b**). At this point, the recombination reaction for H^+ and OH^- dominates the chemical detailed-balance condition and thus the net rate of PAH regeneration via reprotonation of PA^- by H_2O to form OH^- (**Reaction 3f**) must be at a maximum. As $\text{p}K_{\text{a}}$ increases further, the rate of **Reaction 3f** must remain constant while the rate constant increases, and therefore $[\text{PA}^-]_{\text{ss}}$ must decrease under detailed balance. If this did not occur, then the change in chemical potential of PA^- would exceed the maximum change in μ_{OH^-} , as dictated by the net rate of recombination of H^+ and OH^- (**Reaction 1b**), which would exceed generation (Step A). Thus, recombination of H^+ and OH^- dictates $[\text{OH}^-]_{\text{ss}}$, which when it reaches chemical quasi-equilibrium with PA^- , sets the chemical potential of PA^- , and thus $[\text{PA}^-]_{\text{ss}}$, to a value that decreases as $\text{p}K_{\text{a}}$ increases.

Together, these results underscore the importance of isolating effects due to individual parameters when trying to understand complex multistep reactions, as well as the fact that even a

seemingly simple set of reactions (**Reactions 1 – 10**) can result in complicated overall reactivity under specific conditions.

Returning to the model for variable c_{total} and optimal equilibrium pH (pH = 7), we also evaluated realistic conditions, where variations in c_{total} also influence $\text{Abs}_{\text{total}}$. For this we report analogous Nernstian total protonic chemical potential Pareto fronts as three-parameter, two-dimensional plots as ($\text{p}K_{\text{a}}$, $\text{p}K_{\text{a}}^*$ for a series of c_{total}) (**Figure 7c**) and ($\text{p}K_{\text{a}}^*$, c_{total} for a series of $\text{p}K_{\text{a}}$) (**Figure 7d**). (Additional plots showing other combinations of parameters are reported as **Figures S26 – S32**.) These data show that as c_{total} decreases, the range of $\text{p}K_{\text{a}}^*$ values in the zones encompassed by the Pareto fronts decreases, while the range of $\text{p}K_{\text{a}}$ values changes little. Comparing these results with those from the hypothetical model where values of c_{total} did not influence $\text{Abs}_{\text{total}} = 1$, as expected, as c_{total} decreases the rate of light absorption (Step A) decreases, which in turn decreases the steady-state concentrations, and thus chemical potentials, of H^+ and/or OH^- (**Figures S30 and S31**). However, more interestingly, the beneficial effects of decreasing c_{total} (**Figures 7a,b and 8**) are almost exactly offset by the detrimental effects of decreasing c_{total} on absorption, and thus generation rate, to result in a range of $\text{p}K_{\text{a}}$ values in the zones encompassed by the Pareto fronts that are nearly constant, although c_{total} values range from 100 μM to 1 M (**Figure 7c**). Practically, this means that at optimal equilibrium pH (pH = 7), decreasing c_{total} for dyes with $\text{p}K^* \approx 0$ does not require that $\text{p}K$ increase in order to compensate for less light absorption, thus allowing a range of total dye concentrations to be used without detrimental effects on the sum of the steady-state chemical potentials for H^+ and OH^- . However, the projected short-circuit photocurrent density, and therefore sunlight-to-protonic power conversion efficiency, will decrease nearly linearly with c_{total} over the range of values examined, indicating that a large value of c_{total} , and thus $\text{Abs}_{\text{total}}$, is still strongly favored for efficient sunlight-to-protonic power

conversion. For this reason, we simulated the only other case that could achieve a reasonable efficiency, i.e. $c_{\text{total}} = 0.1 \text{ M}$, using the model that included rigorous thermal detailed-balance conditions, and, as before, simulation results were nearly unchanged from those obtained for the base-case model (**Figure S10b**).

Impacts of results on the ability of ESPT to be used for sunlight-to-protonic photochemical power conversion

Results reported above indicate that under conditions of solar irradiation, the sum of the steady-state chemical potentials for $\text{H}^+(\text{aq})$ and $\text{OH}^-(\text{aq})$ can be equal to approximately half of the value observed for mobile electrons and holes in high-quality crystalline silicon photovoltaics.⁶¹ However, these changes in total protonic chemical potential require near-optimal sunlight absorption by photoacids or photobases over a very thin 10 nm distance. While this distance is consistent with the width of the space-charge region reported for commercial bipolar membranes,^{32,35} and may suggest this is an ideal distance to target for having near-complete light absorption, photoacid and/or photobase dyes that exhibit such strong and panchromatic visible-light absorption do not exist, thus necessitating further research into the development of next-generation dyes. Based on the absorption properties of current photoacids and photobases, maximum rates of photochemical processes will only be $\sim 10\%$ of the values resulting from our simulations, which corresponds to a decrease in the sum of the steady-state chemical potentials for $\text{H}^+(\text{aq})$ and $\text{OH}^-(\text{aq})$ by a Nernstian shift of $\sim 59.2 \text{ meV}$. This dilution of photoexcitation events also occurs when the optical pathlength over which light is absorbed or the reactor volume inputted into COMSOL Multiphysics is increased (**Figure S1d,e**). Nevertheless, for photogeneration of minority carrier protonic water species, which are critical to the observation of large total protonic

chemical potentials, photoacids and photobases should exhibit approximately $|\Delta pK| > 8$, with pK and pK^* values that straddle 7. To our knowledge, detailed experimental validation of dyes with these values^{47,52,62,63} and that undergo the Förster cycle mechanism⁶⁴ have not been reported in the literature, and thus attaining such values requires careful consideration of theoretical designs and synthetic strategies. However, target $|\Delta pK|$ values also decrease logarithmically with increase in excited-state lifetime of the dyes, implying that longer-lived excited states, which are typical for inorganic coordination compound or metastable cis–trans isomerization dye molecules,^{65–67} may relax this design requirement. Interestingly, total dye concentration is also an important consideration in predicting total protonic chemical potential, where in some cases lowering the total dye concentration did not impact performance. This suggests that development of more strongly absorbing photoacid and photobase dyes may be important depending on ultimate design considerations for sunlight-to-protonic photochemical power conversion, where having a lower total dye concentration may be important. Although, an increase in molar absorptivity results in a decrease in excited-state lifetime, which is detrimental to overall performance (**Figure 6**). Notwithstanding, even with the many challenges that remain in the development of photoacid and photobase dyes with properties that enable generation of significant changes in protonic chemical potentials, the field is ripe for discovery. This is because little effort has been devoted to developing strongly absorbing panchromatic photoacid and photobase dyes with long-lived excited states and large changes in pK upon photon absorption.

Conclusions

Detailed-balance efficiency limits for sunlight-to-protonic power conversion using photoacid/photobase-sensitized water as the protonic semiconductor were simulated for the first

time using a chemical kinetics model. Given reasonable assumptions, the maximum possible power conversion efficiency was determined to be $\sim 10\%$ and the maximum possible photovoltage was determined to be ~ 330 mV, which occur for photoacids (photobases) with pK_a (pK_b) = 0 and pK_a^* (pK_b^*) = 14 and are optimal when equilibrium pH = 7. Photogeneration of minority carrier protonic water species, i.e. H^+ at equilibrium pH > 7 and OH^- at equilibrium pH < 7 , are primarily responsible for the largest changes in steady-state chemical potentials for H^+ and/or OH^- mobile charged species that enable performance of useful work. Longer excited-state lifetimes allow for more flexibility in the choice of pK_a and pK_a^* , up until ~ 1 μs , where after that the sum of the steady-state chemical potentials for H^+ and OH^- decreases due to large photoinduced changes in equilibrium pH or pOH values. While large concentrations of photoacid or photobase dyes are generally found to be beneficial for sunlight-to-protonic energy conversion, the total dye concentration does not influence optimal pK_a values due to opposing effects on light absorption and dye kinetics. Inclusion of rigorous thermal detailed-balance conditions or validated chemical kinetic theories for proton-transfer reactions does not appreciably change outcomes from simulations in comparison to those obtained for the base-case model, except for when proton-transfer rate constants are assumed to increase from the presence of local electric fields, and then the sum of the steady-state chemical potentials for H^+ and OH^- decreases. Together, these data provide guidelines for the design, synthesis, and application of photoacids and photobases for use in devices for light-to-ionic photochemical power conversion.

Acknowledgments

The authors are grateful for financial support from the Gordon and Betty Moore Foundation under a Moore Inventor Fellowship (GBMF grant #5641), Research Corporation for Science

Advancement under a Cottrell Scholar Award (Award #24169), Nissan Chemical Corporation for sponsored research support, and the U.S. Department of Energy Office of Science under an Early Career Research Program Award (DE-SC0019162). We also acknowledge the UCI Chemical, Applied and Materials Physics (ChAMP) Program for COMSOL Multiphysics instruction and support. We are indebted to Prof. Jim Mayer for a conversation with S.A. in December 2018 that led to our detailed understanding of the kinetic rate equations and approximate rate constants of the reported processes. We also thank Simon Luo, Leanna Schulte, and Sam Keene, for helpful and thought-provoking conversations related to this work.

Declaration of Interests

Co-authors are co-inventors on the following pending patent applications that are relevant to this article: US20180065095 and WO2018049061 (S.A.), US20190217255 and WO2019191326 (S.A. and R.B.). S.A. received sponsored research funding support from Nissan Chemical Corporation for work related to that reported in this article.

References

- 1 W. White, C. D. Sanborn, R. S. Reiter, D. M. Fabian and S. Ardo, *J. Am. Chem. Soc.*, 2017, **139**, 11726–11733. DOI: 10.1021/jacs.7b00974.
- 2 W. White, C. D. Sanborn, D. M. Fabian and S. Ardo, *Joule*, 2018, **2**, 94–109. DOI: 10.1016/j.joule.2017.10.015.
- 3 C. D. Sanborn, J. V. Chacko, M. Digman and S. Ardo, *Chem*, 2019, **5**, 1648–1670. DOI: 10.1016/j.chempr.2019.04.022.
- 4 W. White, S. Luo, R. Bhide, C. D. Sanborn, M. S. Baranov, K. M. Solntsev and S. Ardo,

- in *Physical Chemistry of Semiconductor Materials and Interfaces XVIII*, SPIE, 2019, vol. 11084, pp. 110840E1–9. DOI: 10.1117/12.2529900.
- 5 S. Luo, W. White, J. M. Cardon and S. Ardo, *Energy Environ. Sci.*, 2021, **14**, 4961–4978. DOI: 10.1039/d1ee00482d.
 - 6 L. Schulte, W. White, L. A. Renna and S. Ardo, *Joule*, 2021, **5**, 2380–2394. DOI: 10.1016/j.joule.2021.06.016.
 - 7 W. Shockley, *Bell Syst. Tech. J.*, 1949, **28**, 435–489. DOI: 10.1002/j.1538-7305.1949.tb03645.x.
 - 8 C. S. Fuller, *Rec. Chem. Prog.*, 1956, **17**, 75–93.
 - 9 D. M. Chapin, C. S. Fuller and G. L. Pearson, *J. Appl. Phys.*, 1954, **25**, 676–677. DOI: 10.1063/1.1721711.
 - 10 J. Perlin, *Silicon Solar Cell Turns 50*, 1956.
 - 11 W. Shockley and H. J. Queisser, *J. Appl. Phys.*, 1961, **32**, 510–519. DOI: 10.1063/1.1736034.
 - 12 R. T. Ross and T. L. Hsiao, *J. Appl. Phys.*, 1977, **48**, 4783–4785. DOI: 10.1063/1.323494.
 - 13 R. T. Ross, R. J. Anderson and T. L. Hsiao, *Photochem. Photobiol.*, 1976, **24**, 267–278. DOI: 10.1111/j.1751-1097.1976.tb06822.x.
 - 14 J. R. Bolton and M. D. Archer, *J. Phys. Chem.*, 1991, **95**, 8453–8461. DOI: 10.1021/j100175a012.
 - 15 J. R. Bolton, *Science*, 1978, **202**, 705–711. DOI: 10.1126/science.202.4369.705.
 - 16 J. R. Bolton, S. J. Strickler and J. S. Connolly, *Nature*, 1985, **316**, 495–500. DOI: 10.1038/316495a0.
 - 17 K. M. Solntsev, S. A. Al-Ainain, Y. V. Il'ichev and M. G. Kuzmin, *J. Phys. Chem. A*, 2004, **108**, 8212–8222. DOI: 10.1021/jp040201f.
 - 18 J. N. Brønsted and K. Z. Pedersen, *Z. Phys. Chem.*, 1924, **108**, 185–235. DOI: 10.1515/zpch-1924-10814.

- 19 D. Pines and E. Pines, in *Hydrogen-Transfer Reactions: Solvent Assisted Photoacidity*, Wiley-VCH Verlag GmbH & Co. KGaA, Weinheim, Germany, 2007, vol. 1, pp. 377–415. DOI: 10.1002/9783527611546.ch12.
- 20 D. Pines, J. Ditkovich, T. Mukra, Y. Miller, P. M. Kiefer, S. Daschakraborty, J. T. Hynes and E. Pines, *J. Phys. Chem. B*, 2016, **120**, 2440–2451. DOI: 10.1021/acs.jpcc.5b12428.
- 21 R. Bhide, C. N. Feltenberger, G. S. Phun, G. Barton, D. Fishman and S. Ardo, *J. Am. Chem. Soc.*, 2022, **144**, 14477–14488. DOI: 10.1021/jacs.2c00554.
- 22 T. Förster, *Zeitschrift für Elektrochemie*, 1950, **54**, 531–535. DOI: 10.1002/bbpc.19500540707.
- 23 M. Eigen and L. De Maeyer, *Proc. R. Soc. London. Ser. A. Math. Phys. Sci.*, 1958, **247**, 505–533. DOI: 10.1098/rspa.1958.0208.
- 24 A. J. Bard and L. R. Faulkner, *Electrochemical Methods : Fundamentals and Applications*, John Wiley & Sons, Inc., New York, 2nd ed., 1980.
- 25 P. Kapusta, Absolute Diffusion Coefficients: Compilation of Reference Data for FCS Calibration, https://www.picoquant.com/images/uploads/page/files/7353/appnote_diffusioncoefficients.pdf, (accessed 17 August 2020).
- 26 C. Robinson, *Source Proc. R. Soc. London. Ser. A, Math. Phys. Sci.*, 1935, **148**, 681–695. DOI: 10.1098/rspa.1935.0041.
- 27 E. M. Kramer, N. L. Frazer and T. I. Baskin, *J. Exp. Bot.*, 2007, **58**, 3005–3015. DOI: 10.1093/jxb/erm155.
- 28 R. A. Marcus, *J. Phys. Chem.*, 1968, **72**, 891–899. DOI: 10.1021/j100849a019.
- 29 A. O. Cohen and R. A. Marcus, *J. Phys. Chem.*, 1968, **72**, 4249–4256. DOI: 10.1021/j100858a052.
- 30 L. Onsager, *J. Chem. Phys.*, 1934, **2**, 599–615. DOI: 10.1063/1.1749541.
- 31 R. Simons, *Nature*, 1979, **280**, 824–826. DOI: 10.1038/280824a0.

- 32 N. P. Craig, Ph.D. Dissertation, University of California, Berkeley, 2013.
- 33 NREL, Reference Air Mass 1.5 Spectra | Grid Modernization | NREL, <https://www.nrel.gov/grid/solar-resource/spectra-am1.5.html>, (accessed 21 August 2020).
- 34 S. M. Sze and K. K. Ng, *Physics of Semiconductor Devices*, John Wiley & Sons, Inc., 2006.
- 35 M. Ünlü, J. Zhou and P. A. Kohl, *J. Phys. Chem. C*, 2009, **113**, 11416–11423. DOI: 10.1021/jp903252u.
- 36 H. P. Soroka, R. Simkovitch, A. Kosloff, S. Shomer, A. Pevzner, O. Tzang, R. Tirosh, F. Patolsky and D. Huppert, *J. Phys. Chem. C*, 2013, **117**, 25786–25797, DOI: 10.1021/jp4087514.
- 37 O. Gajst, L. Pinto da Silva, J. C. G. Esteves da Silva and D. Huppert, *J. Phys. Chem. A*, 2018, **122**, 6166–6175, DOI: 10.1021/acs.jpca.8b04417.
- 38 K. M. Solntsev, D. Huppert, N. Agmon and L. M. Tolbert, *J. Phys. Chem. A*, 2000, **104**, 4658–4669. DOI: 10.1021/jp994454y.
- 39 K. Tkaczibson and S. Ardo, *Sustain. Energy Fuels*, 2019, **3**, 1573–1587. DOI: 10.1039/c9se00009g.
- 40 J. C. Chang, C. J. Ma, G. H. Lee, S. M. Peng and C. Y. Yeh, *Dalt. Trans.*, 2005, 1504–1508. DOI: 10.1039/b417350c.
- 41 T. Higashino and H. Imahori, *Dalt. Trans.*, 2015, **44**, 448–463. DOI: 10.1039/c4dt02756f.
- 42 W. W. Yu, L. Qu, W. Guo and X. Peng, *Chem. Mater.*, 2003, **15**, 2854–2860. DOI: 10.1021/cm034081k.
- 43 R. Bala Chandran, S. Breen, Y. Shao, S. Ardo and A. Z. Weber, *Energy Environ. Sci.*, 2018, **11**, 115–135. DOI: 10.1039/c7ee01360d.
- 44 J. R. Lakowicz, *Principles of Fluorescence Spectroscopy*, Springer, Boston, MA, 3rd ed., 2006.
- 45 I. Vlassioux and Z. S. Siwy, *Nano Lett.*, 2007, **7**, 552–556. DOI: 10.1021/nl062924b.

- 46 D. Constantin and Z. S. Siwy, *Phys. Rev. E - Stat. Nonlinear, Soft Matter Phys.*, 2007, **76**, 041202. DOI: 10.1103/PhysRevE.76.04120.
- 47 I. Y. Martynov, A. B. Demyashkevich, B. M. Uzhinov and M. G. Kuz'min, *Russ. Chem. Rev.*, 1977, **46**, 1–15. DOI: 10.1070/rc1977v046n01abeh002116.
- 48 C. Hicks, G. Ye, C. Levi, M. Gonzales, I. Rutenburg, J. Fan, R. Helmy, A. Kassis and H. D. Gafney, *Coord. Chem. Rev.*, 2001, **211**, 207–222. DOI: 10.1016/S0010-8545(00)00279-4.
- 49 L. M. Tolbert and J. E. Haubrich, *J. Am. Chem. Soc.*, 1994, **116**, 10593–10600. DOI: 10.1021/ja00102a028.
- 50 S.-Y. Park, Y. M. Lee, K. Kwac, Y. Jung and O.-H. Kwon, *Chem. - A Eur. J.*, 2016, **22**, 4340–4344. DOI: 10.1002/chem.201503948.
- 51 K. Schäfer, H. Ihmels, C. Bohne, K. P. Valente and A. Granzhan, *J. Org. Chem.*, 2016, **81**, 10942–10954. DOI: 10.1021/acs.joc.6b01991.
- 52 E. W. Driscoll, J. R. Hunt and J. M. Dawlaty, *J. Phys. Chem. Lett.*, 2016, **7**, 2093–2099. DOI: 10.1021/acs.jpcclett.6b00790.
- 53 Z. Wen, L. J. Karas, C.-H. Wu and J. I.-C. Wu, *Chem. Commun*, 2020, **56**, 8380–8383. DOI: 10.1039/d0cc02952a.
- 54 M. A. Green, *Solid State Electron.*, 1981, **24**, 788–789. DOI: 10.1016/0038-1101(81)90062-9.
- 55 S. Fonash, *Solar Cell Device Physics*, Elsevier, Burlington, MA, 2nd ed., 2010.
- 56 M. C. Hanna and A. J. Nozik, *J. Appl. Phys.*, 2006, **100**, 0745101–0745108. DOI: 10.1063/1.2356795.
- 57 R. Simkovitch, S. Shomer, R. Gepshtein and D. Huppert, *J. Phys. Chem. B*, 2015, **119**, 2253–2262. DOI: 10.1021/jp506011e.
- 58 S. J. Strickler and R. A. Berg, *J. Chem. Phys.*, 1962, **37**, 814–822. DOI: 10.1063/1.1733166.

- 59 B. Bensaid, F. Raymond, M. Leroux, C. Vèrié and B. Fofana, *J. Appl. Phys.*, 1989, **66**, 5542–5548. DOI: 10.1063/1.343658.
- 60 J. E. Parrott, *Sol. Energy Mater. Sol. Cells*, 1993, **30**, 221–231. DOI: 10.1016/0927-0248(93)90142-P.
- 61 M. Green, E. Dunlop, J. Hohl-Ebinger, M. Yoshita, N. Kopidakis and X. Hao, *Prog. Photovoltaics Res. Appl.*, 2021, **29**, 3–15. DOI: 10.1002/pip.3371.
- 62 D. J. Stewart, J. J. Concepcion, M. K. Brennaman, R. A. Binstead and T. J. Meyer, *Proc. Natl. Acad. Sci. U. S. A.*, 2013, **110**, 876–880. DOI: 10.1073/pnas.1220742110.
- 63 B. Finkler, C. Spies, M. Vester, F. Walte, K. Omlor, I. Riemann, M. Zimmer, F. Stracke, M. Gerhards and G. Jung, *Photochem. Photobiol. Sci.*, 2014, **13**, 548–562. DOI:10.1039/c3pp50404b.
- 64 S. Roy, S. Ardo and F. Furche, *J. Phys. Chem. A*, 2019, **123**, 6645–6651. DOI: 10.1021/acs.jpca.9b05341.
- 65 A. Juris, V. Balzani, F. Barigelletti, S. Campagna, P. Belser and A. von Zelewsky, *Coord. Chem. Rev.*, 1988, **84**, 85–277. DOI: 10.1016/0010-8545(88)80032–8.
- 66 R. M. O’Donnell, R. N. Sampaio, G. Li, P. G. Johansson, C. L. Ward and G. J. Meyer, *J. Am. Chem. Soc.*, 2016, **138**, 3891–3903. DOI: 10.1021/jacs.6b00454.
- 67 Y. Liao, *Acc. Chem. Res.*, 2017, **50**, 1956–1964. DOI: 10.1021/acs.accounts.7b00190.